Fig. 5.1.5: Same as figure 5.1.2 for Norrköping, Sweden.
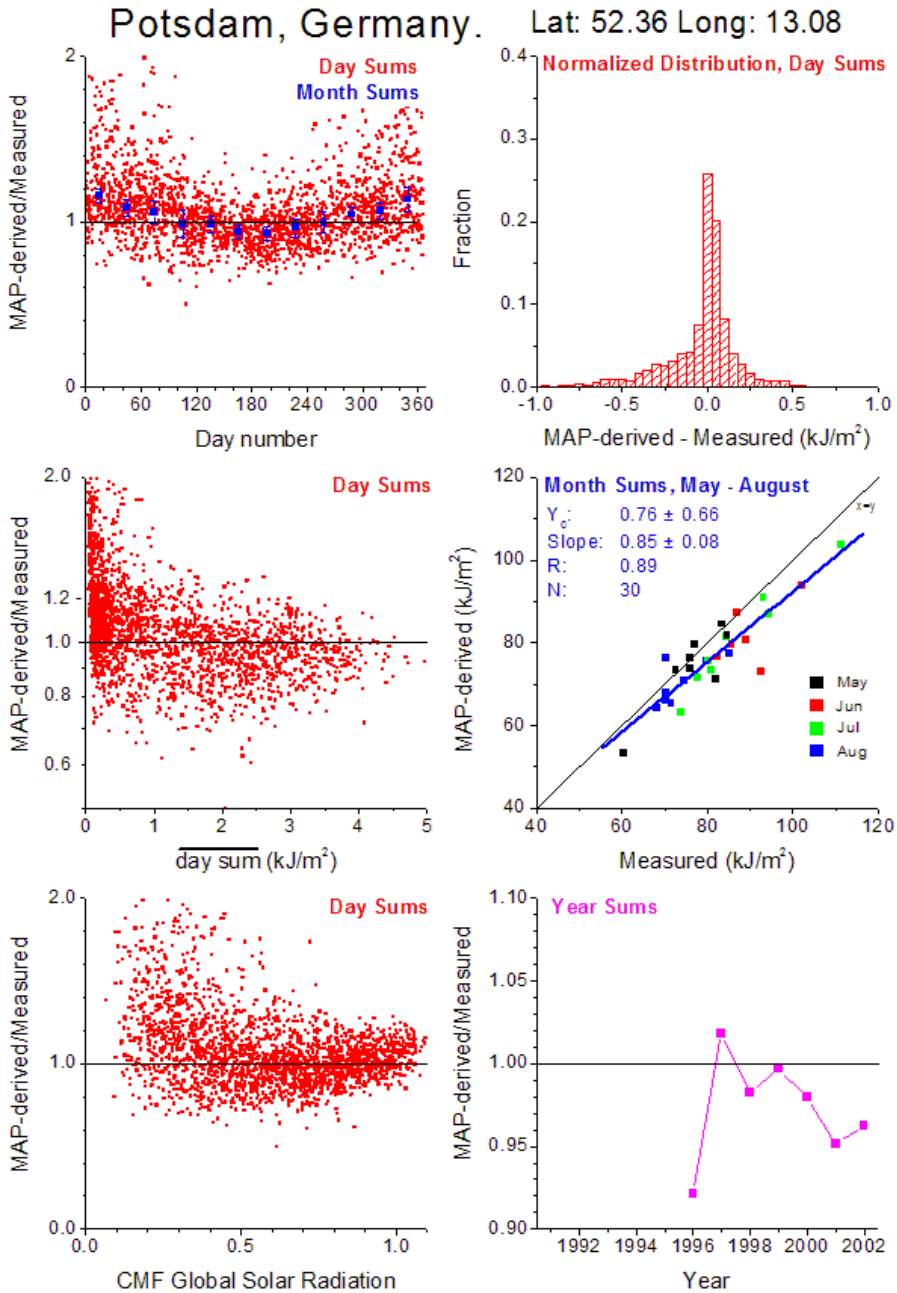
Fig. 5.1.6: Same as figure 5.1.2 for Potsdam, Germany.
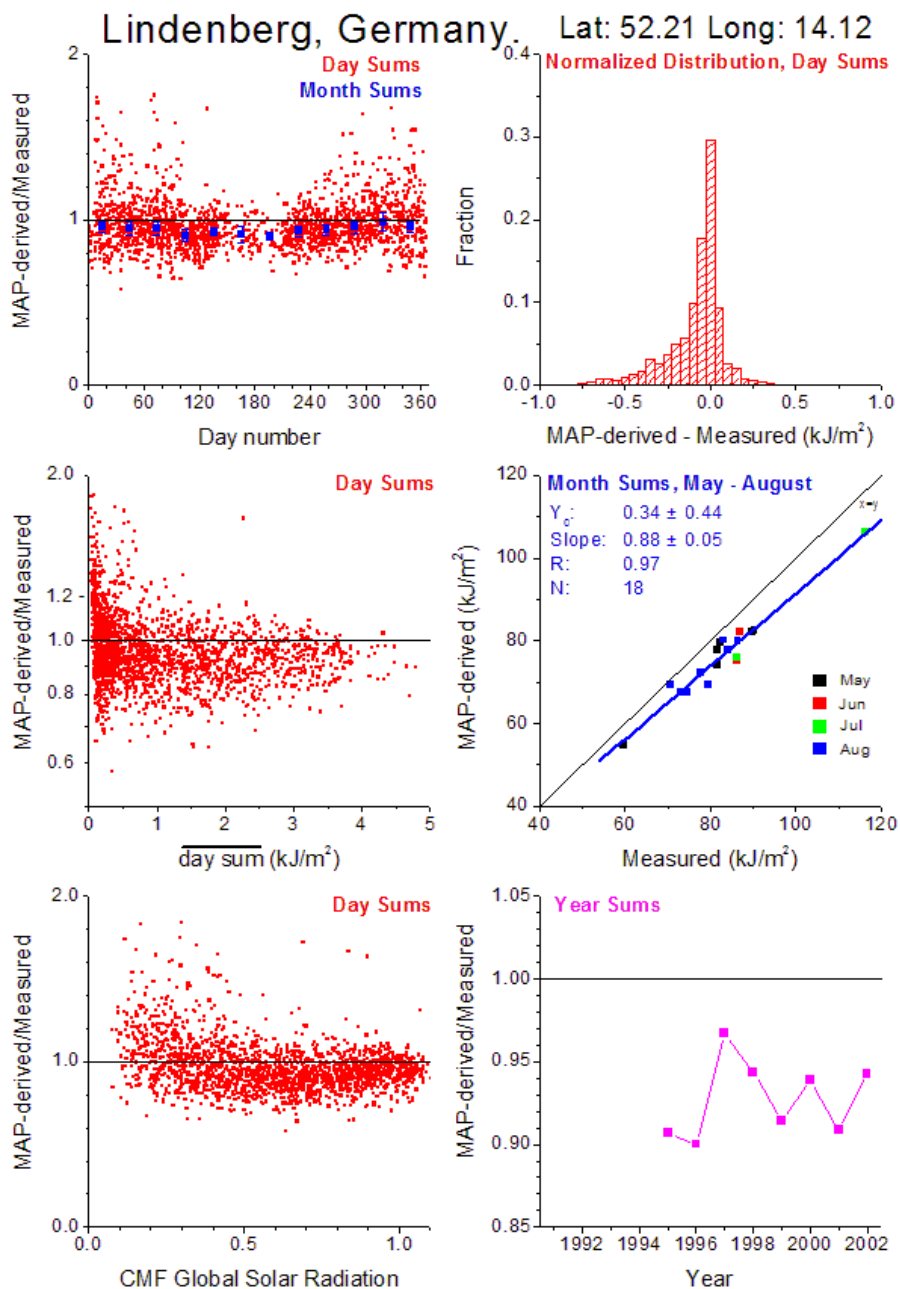
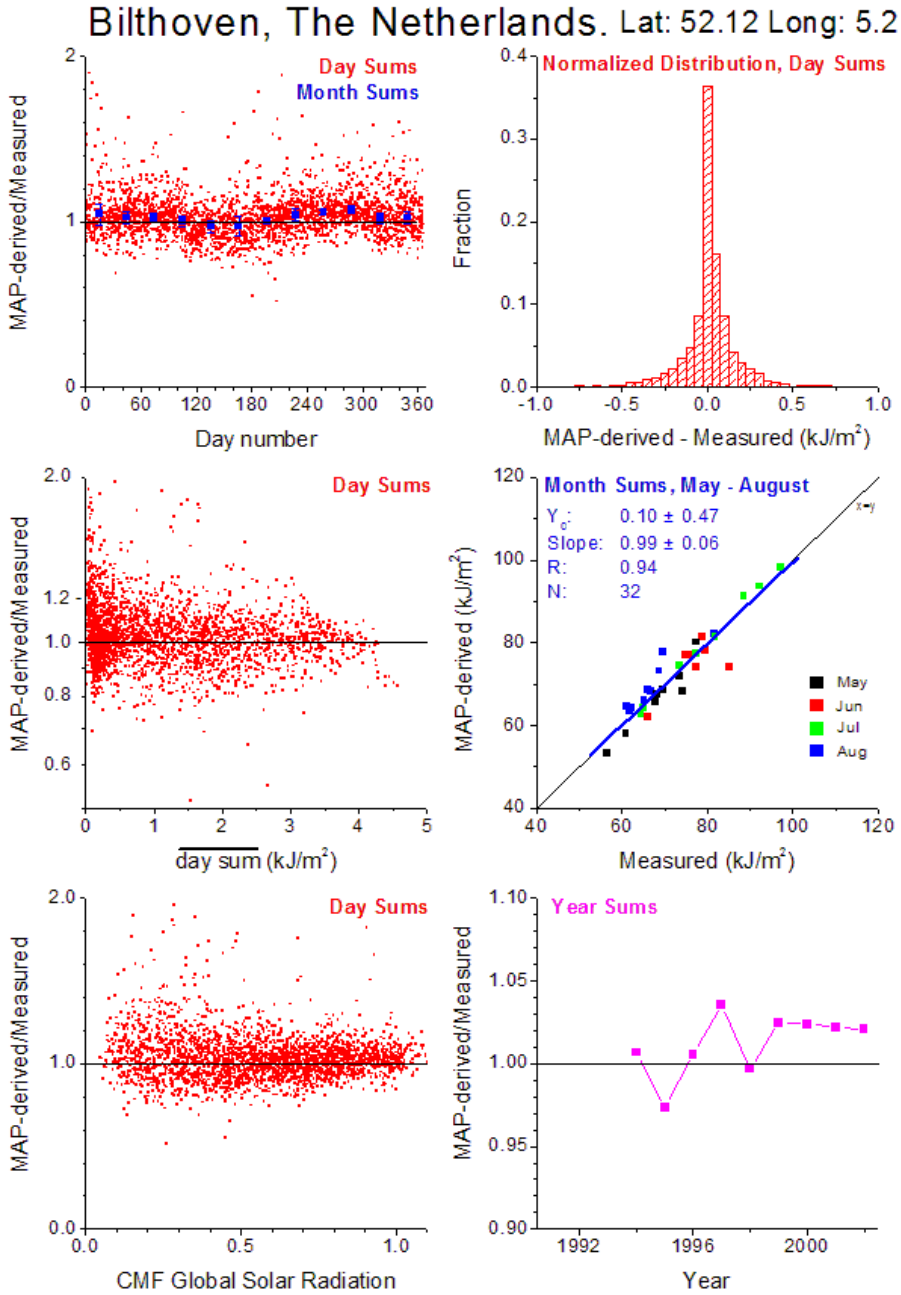**Fig. 5.1.7**: Same as figure 5.1.2 for Lindenberg, Germany.

Fig. 5.1.8: Same as figure 5.1.2 for Bilthoven, The Netherland.
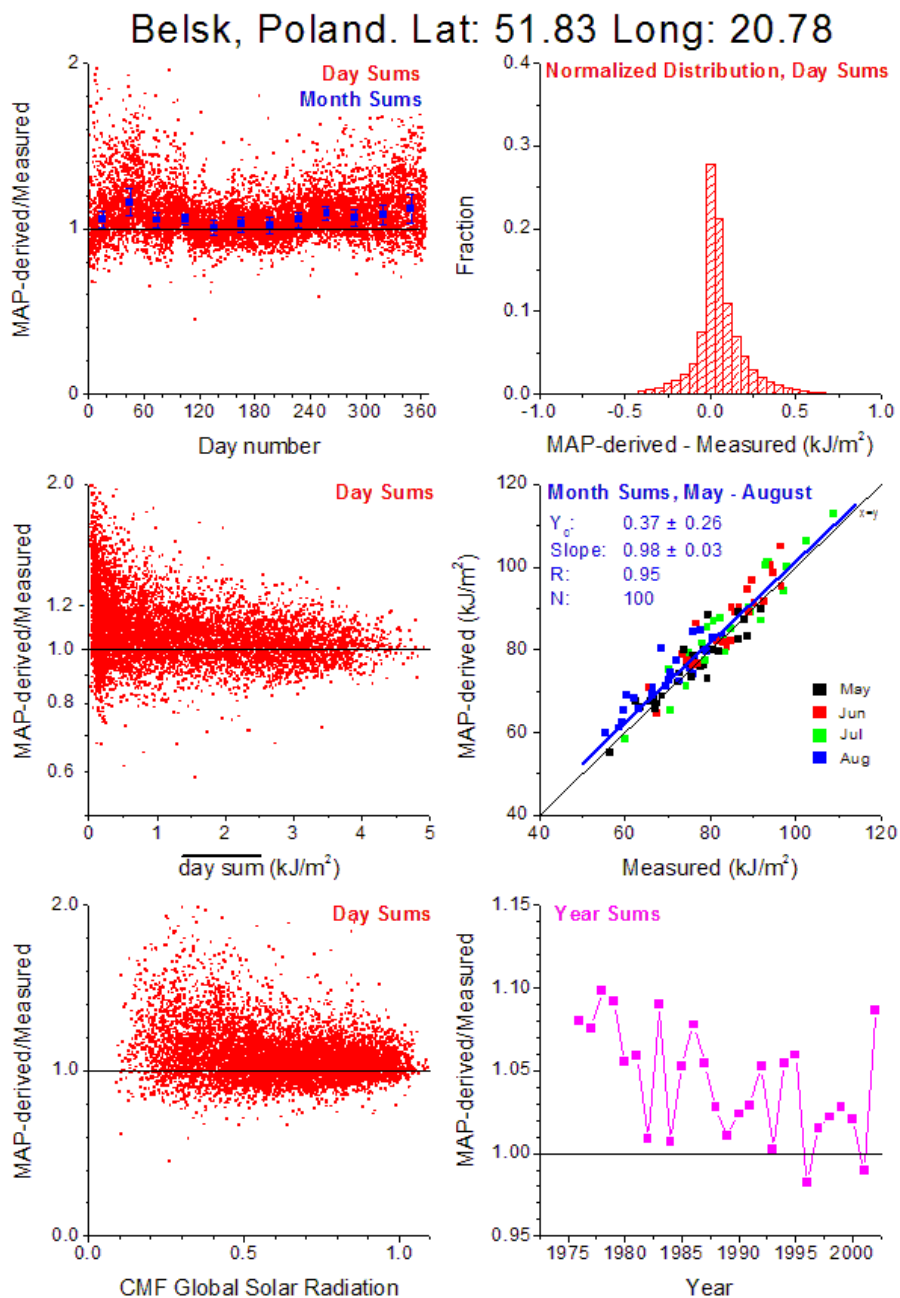
Fig. 5.1.9: Same as figure 5.1.2 for Belsk, Poland.
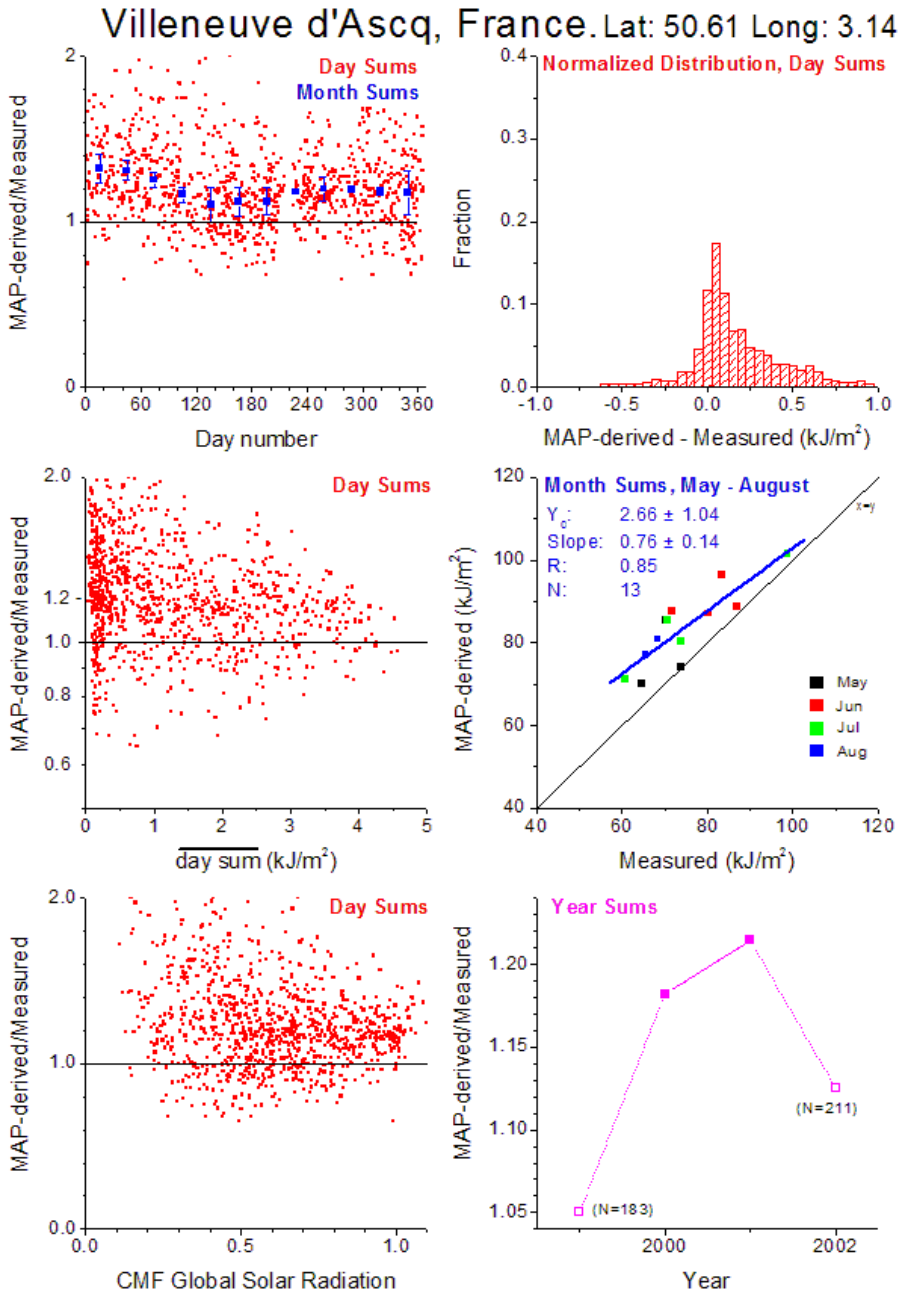
Fig. 5.1.10: Same as figure 5.1.2 for Villeneuve d'Ascq, France.
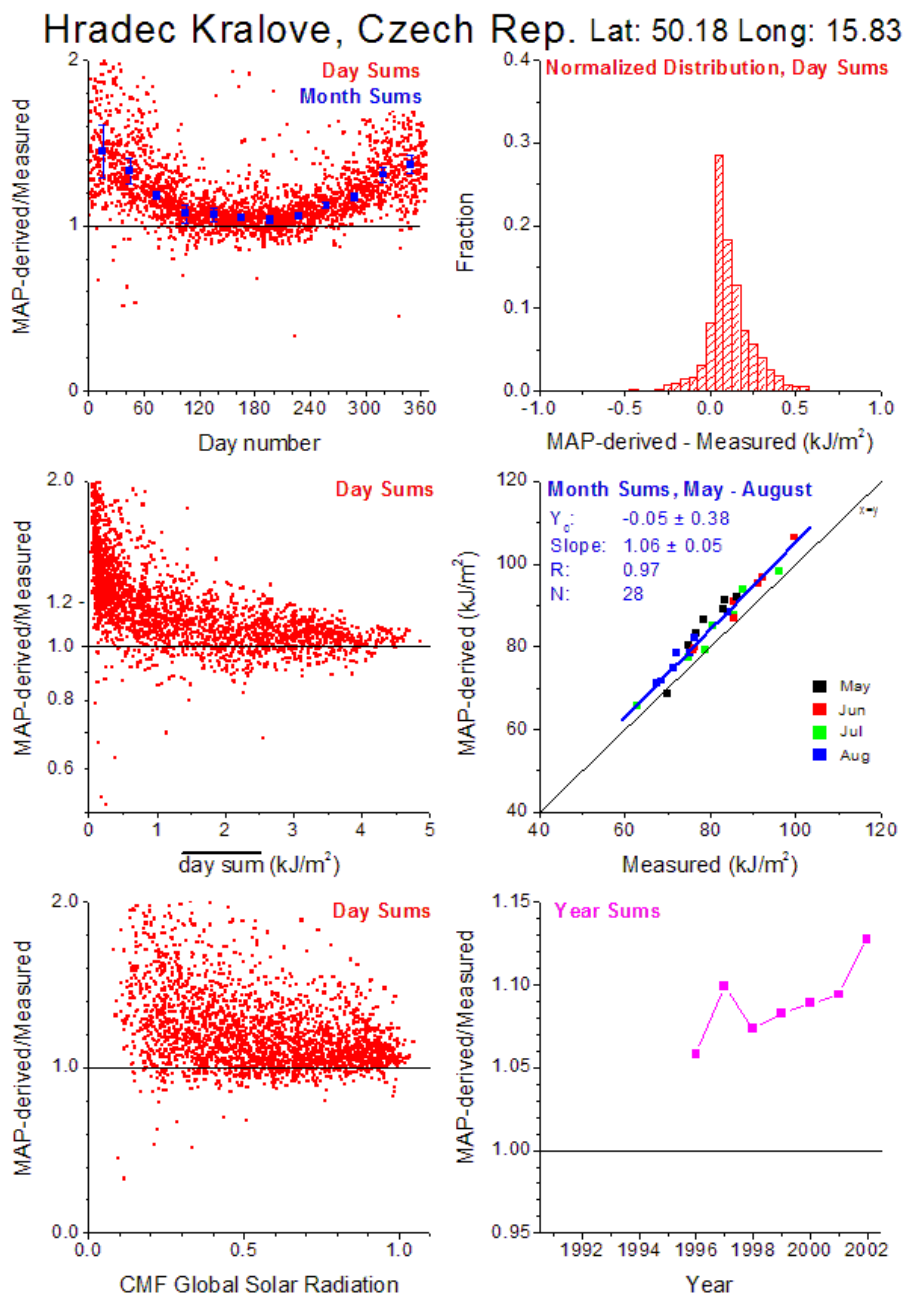
Fig. 5.1.11: Same as figure 5.1.2 for Hradec Kralove, Czech Republic.
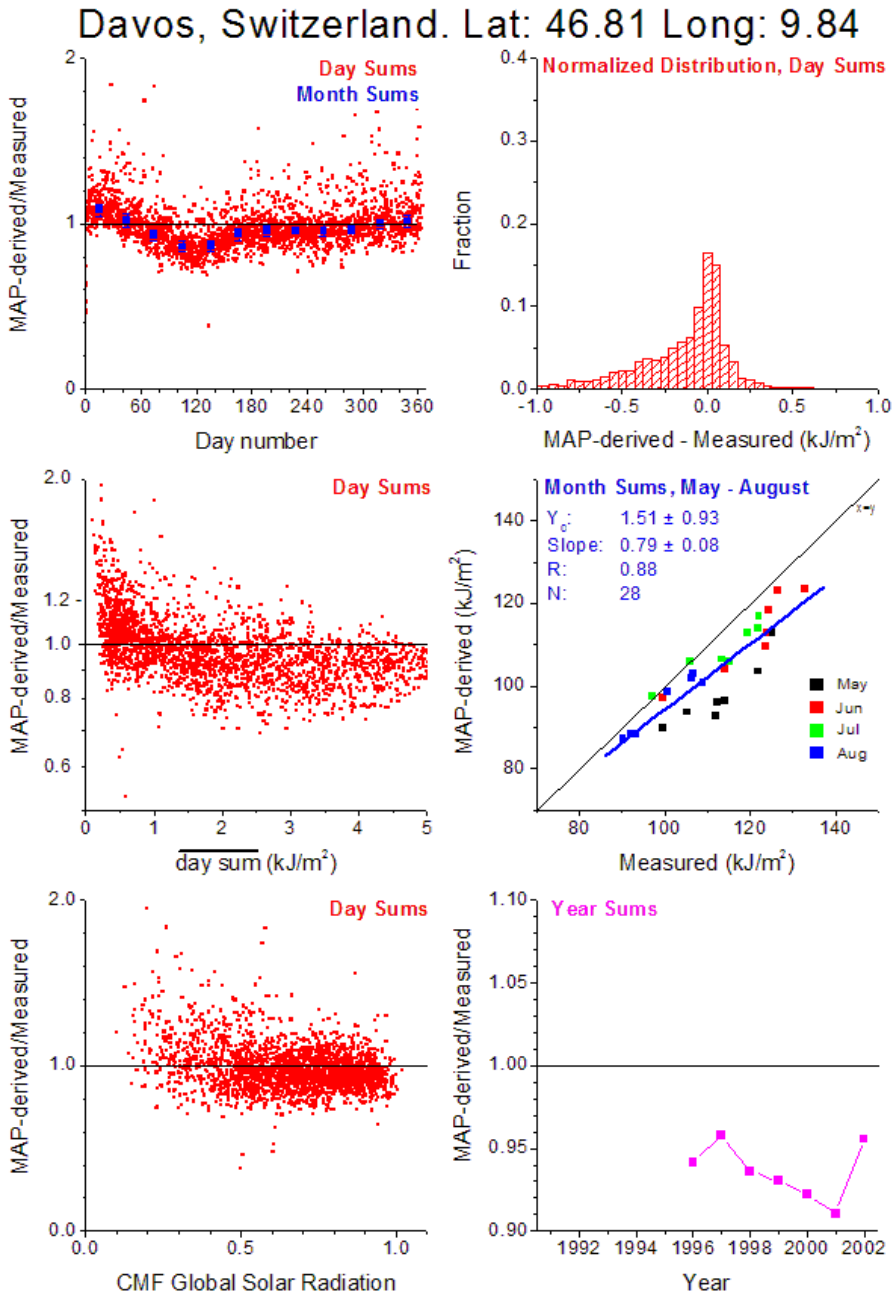
Fig. 5.1.12: Same as figure 5.1.2 for Davos, Switzerland.
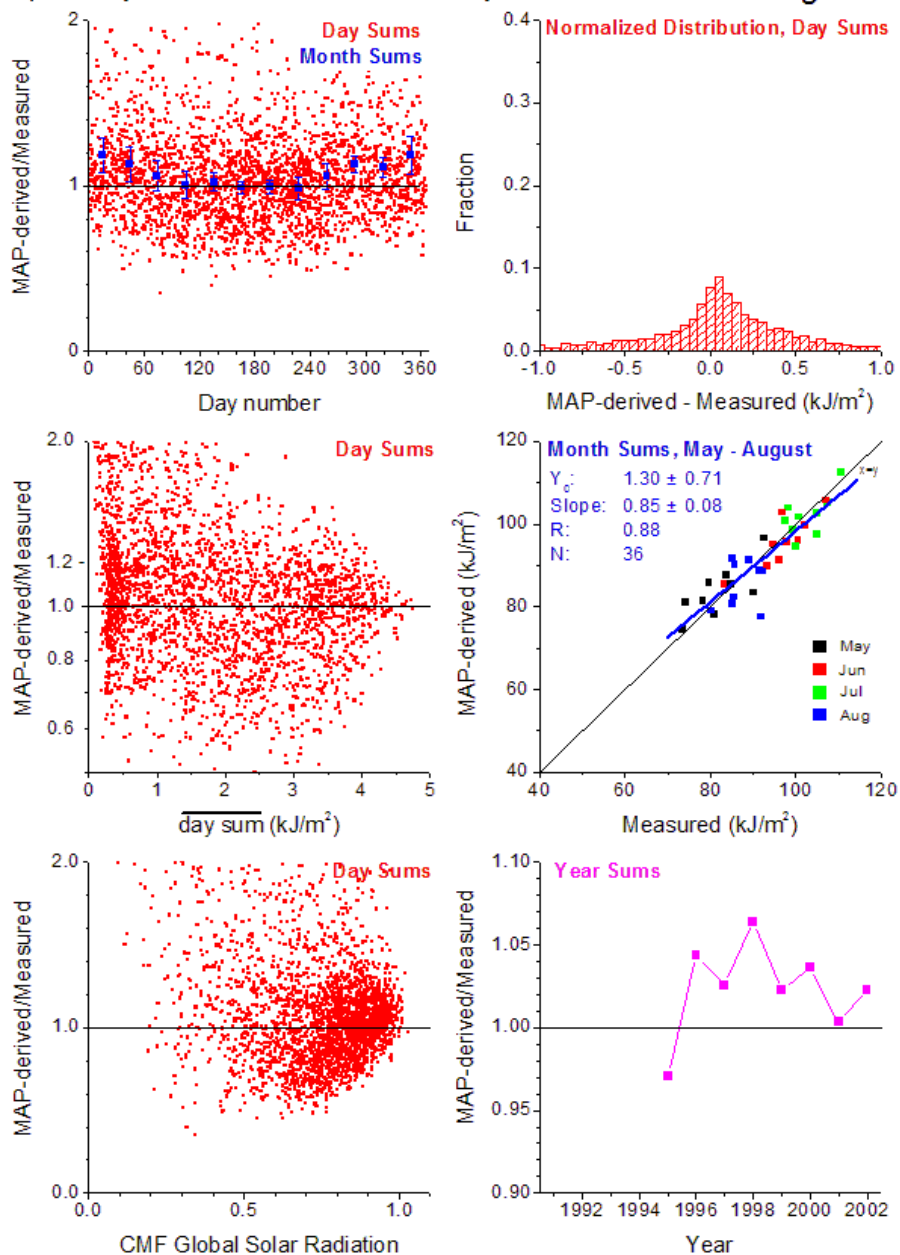
Fig. 5.1.13: Same as figure 5.1.2 for Ispra, Italy.
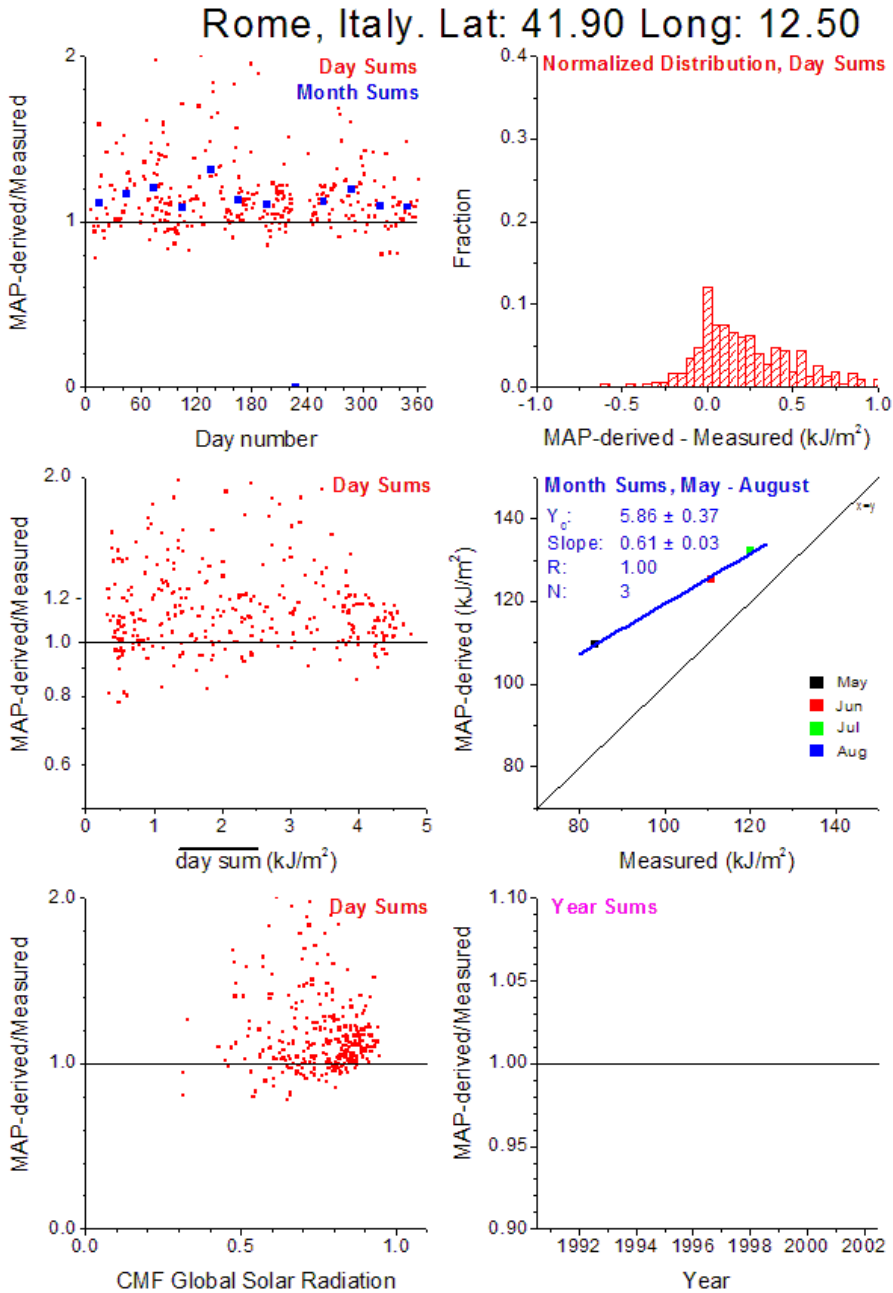
Fig. 5.1.14: Same as figure 5.1.2 for Rome, Italy.
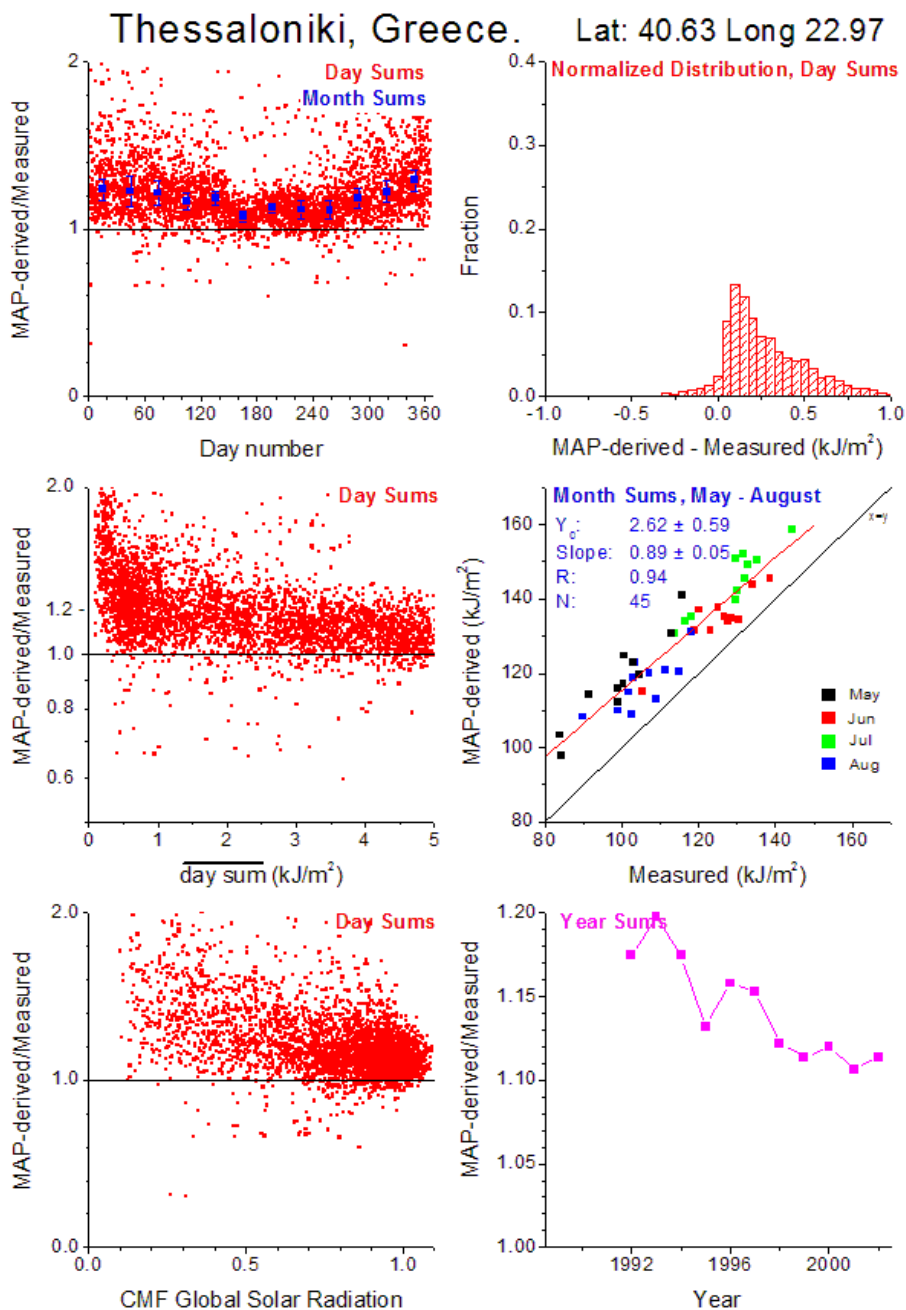
Fig. 5.1.15: Same as figure 5.1.2 for Thessaloniki, Grece
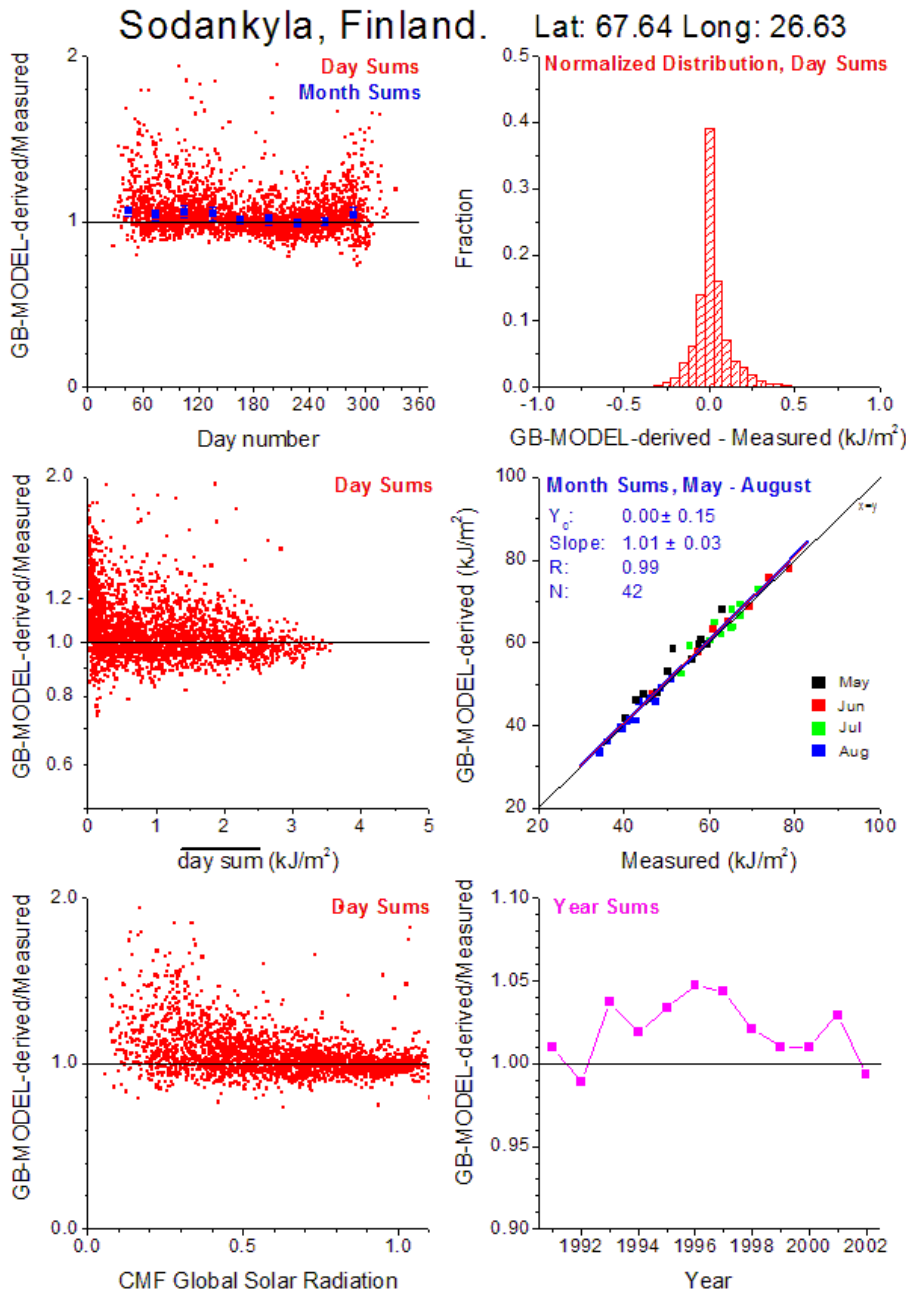
Fig. 5.1.16: Detailed results for the comparison of measured and modelled UV-doses. Results are for ground based modelling using the RIVM model technique (den Outer, 2005) for Sodankyla, Finland.
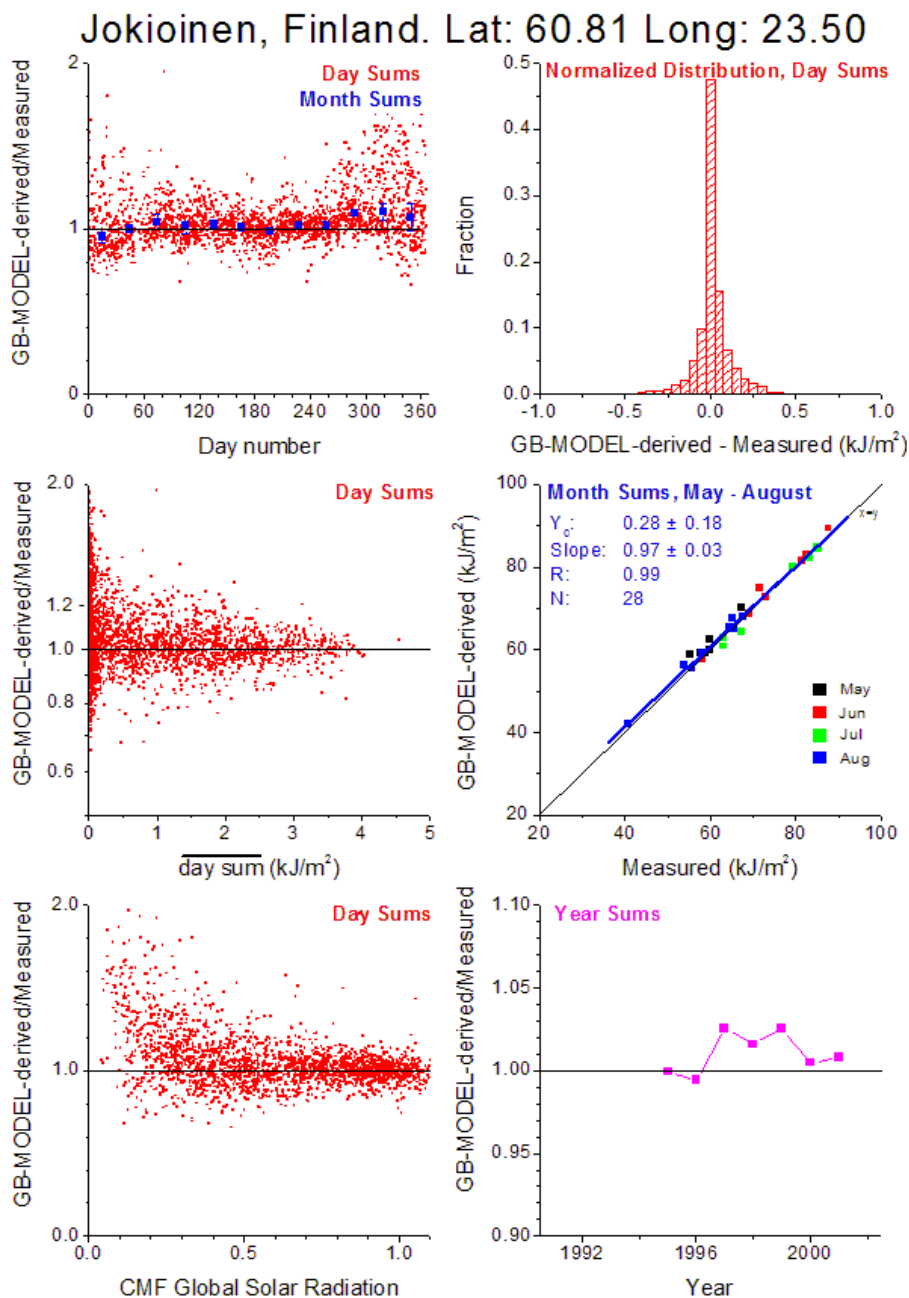
Fig. 5.1.17: Same as figure 5.1.16 for Jokioinen, Finland.
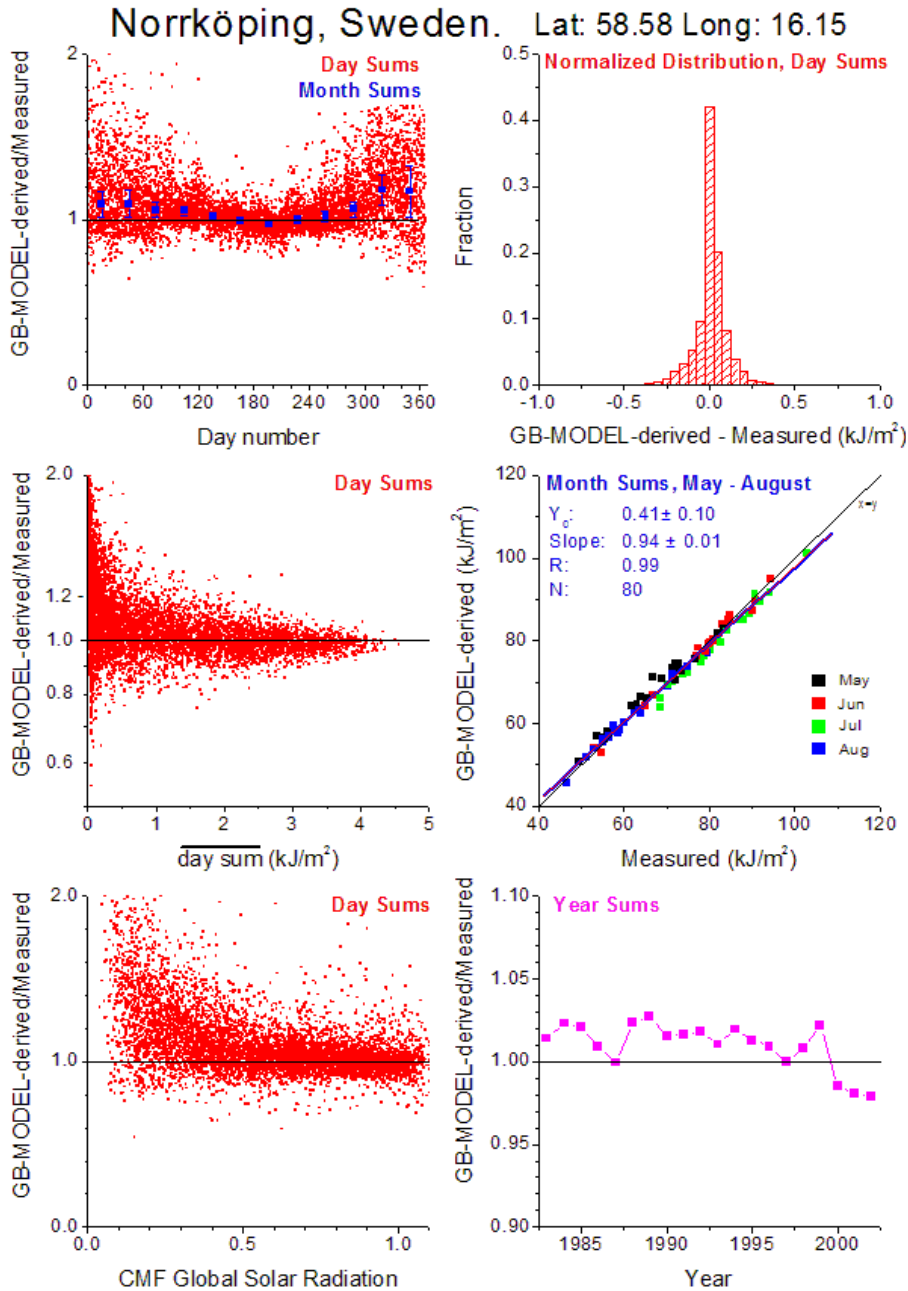
Fig. 5.1.18: Same as figure 5.1.16 for Norrköping, Sweden.
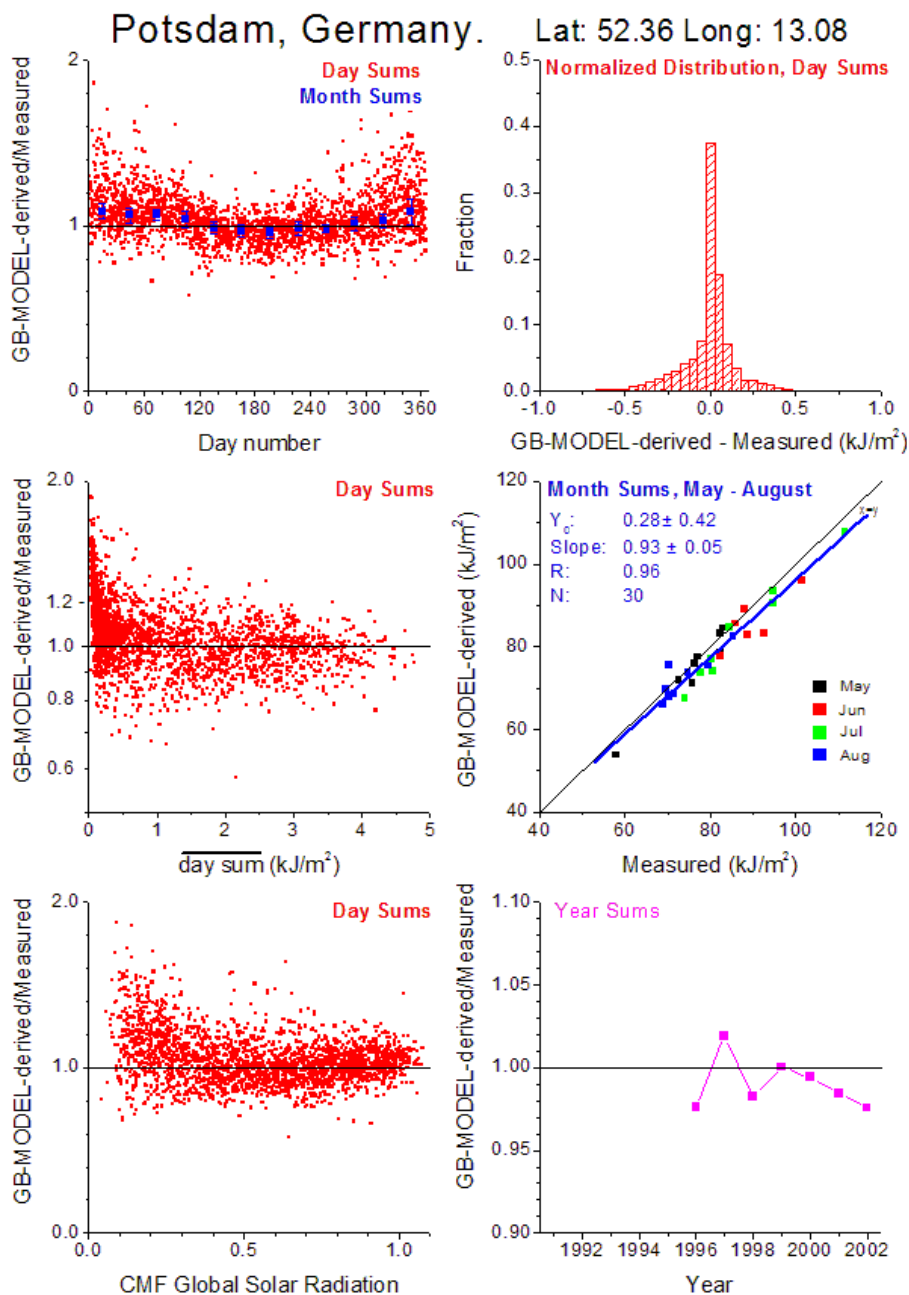
Fig. 5.1.19: Same as figure 5.1.16 for Potsdam, Germany.
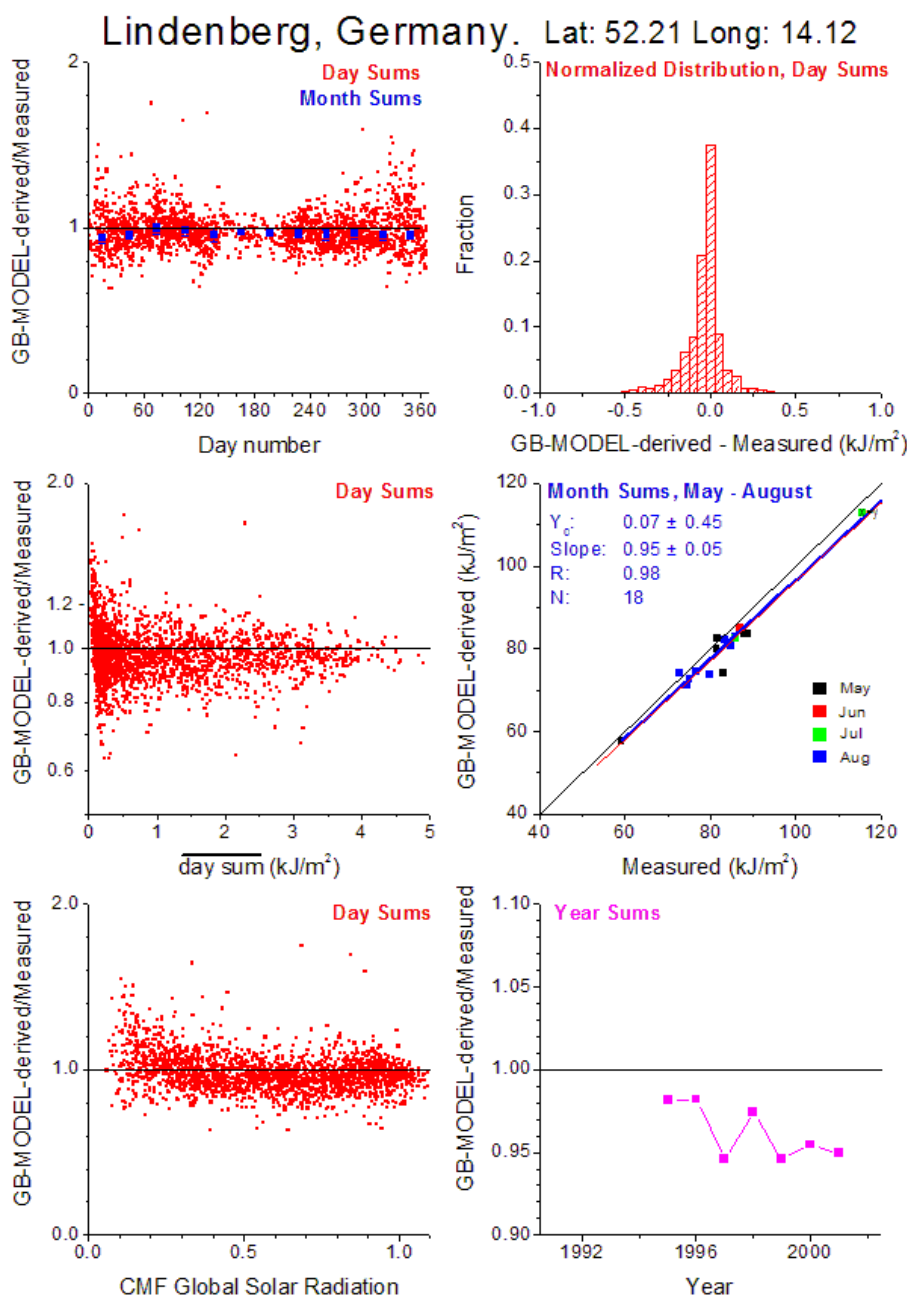
Fig. 5.1.20: Same as figure 5.1.16 for Lindenberg, Germany.
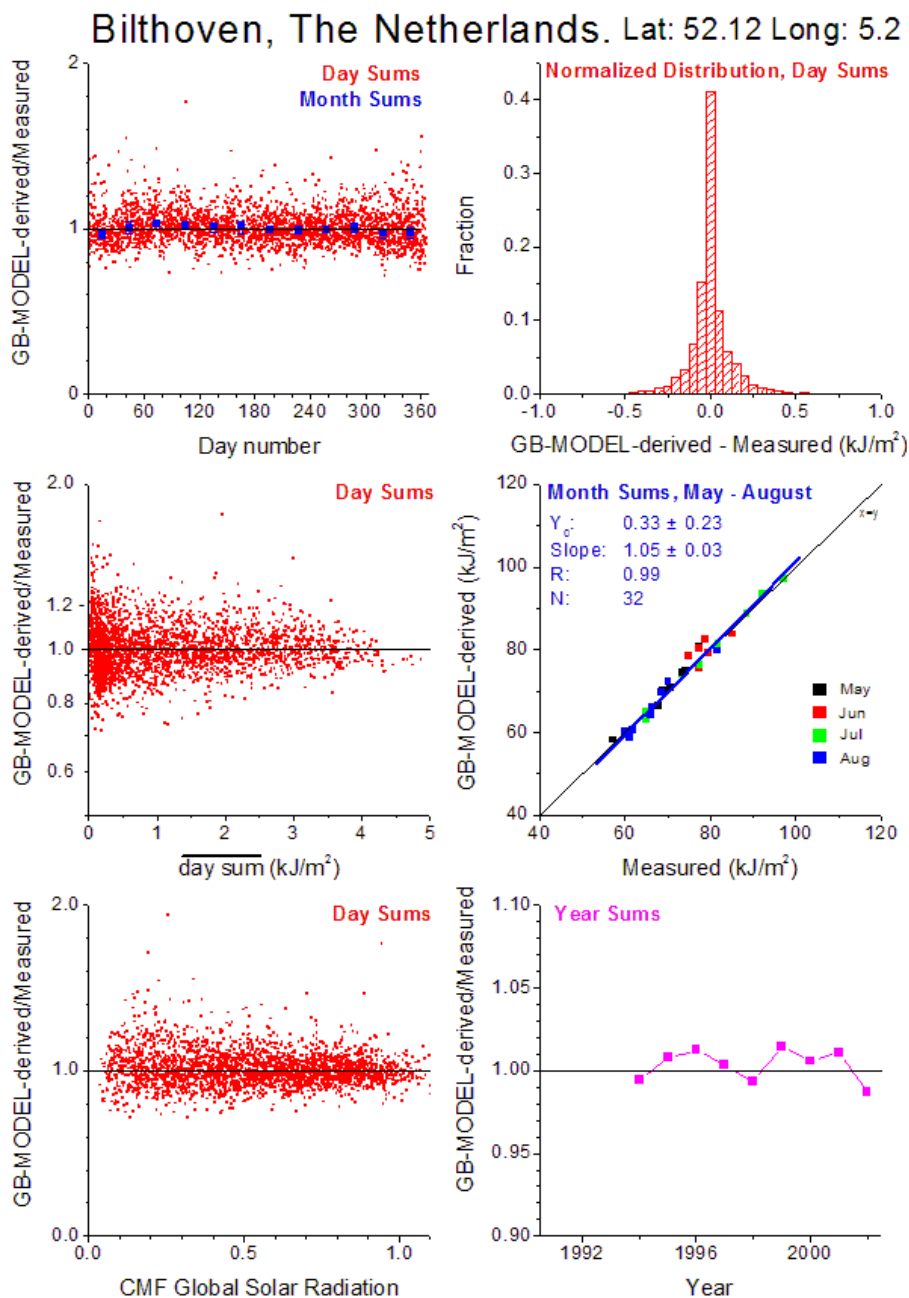
Fig. 5.1.21: Same as figure 5.1.16 for Bilthoven, The Netherland.
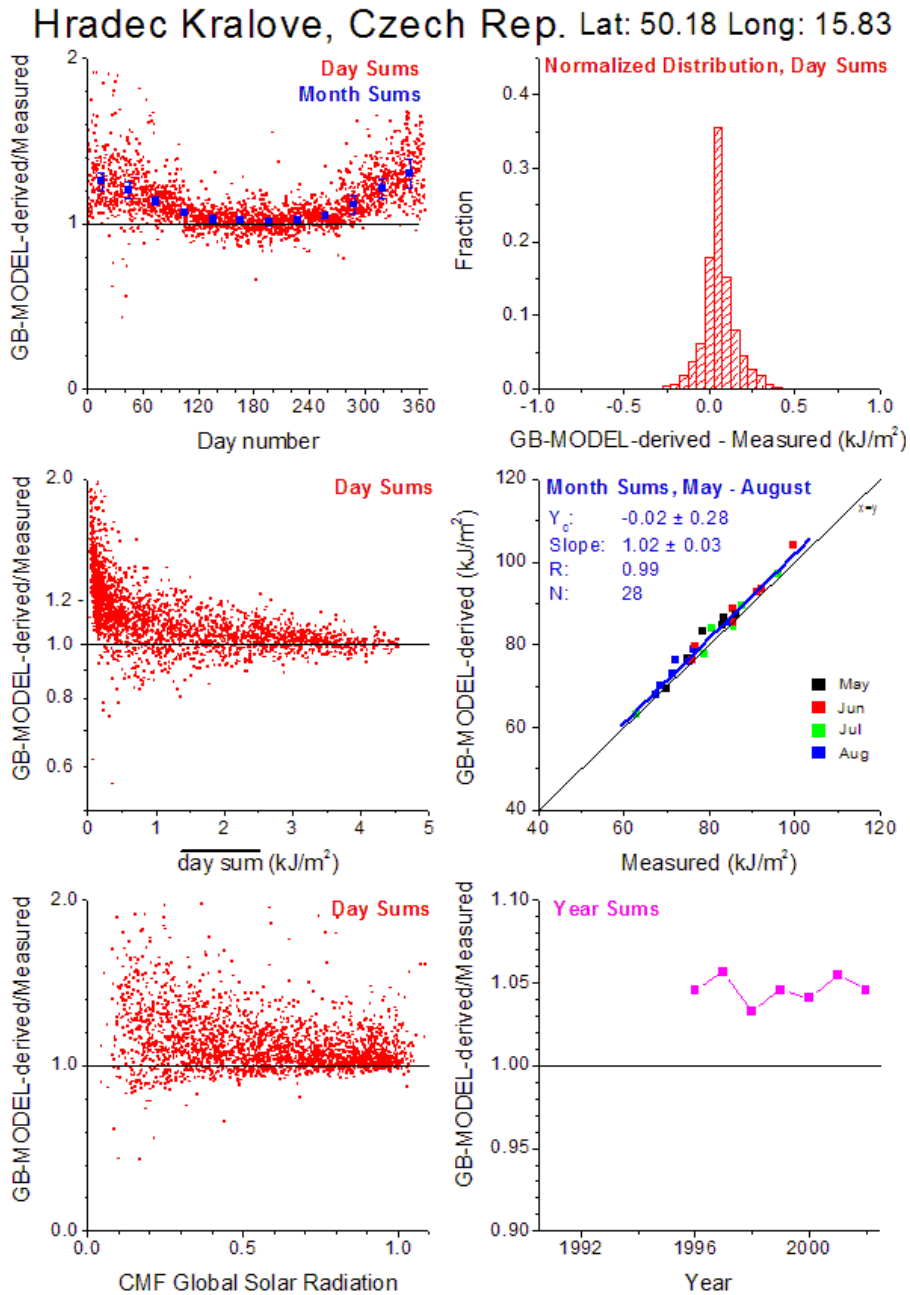
Fig. 5.1.22: Same as figure 5.1.16 for Hradec Kralove, Czech Republic.
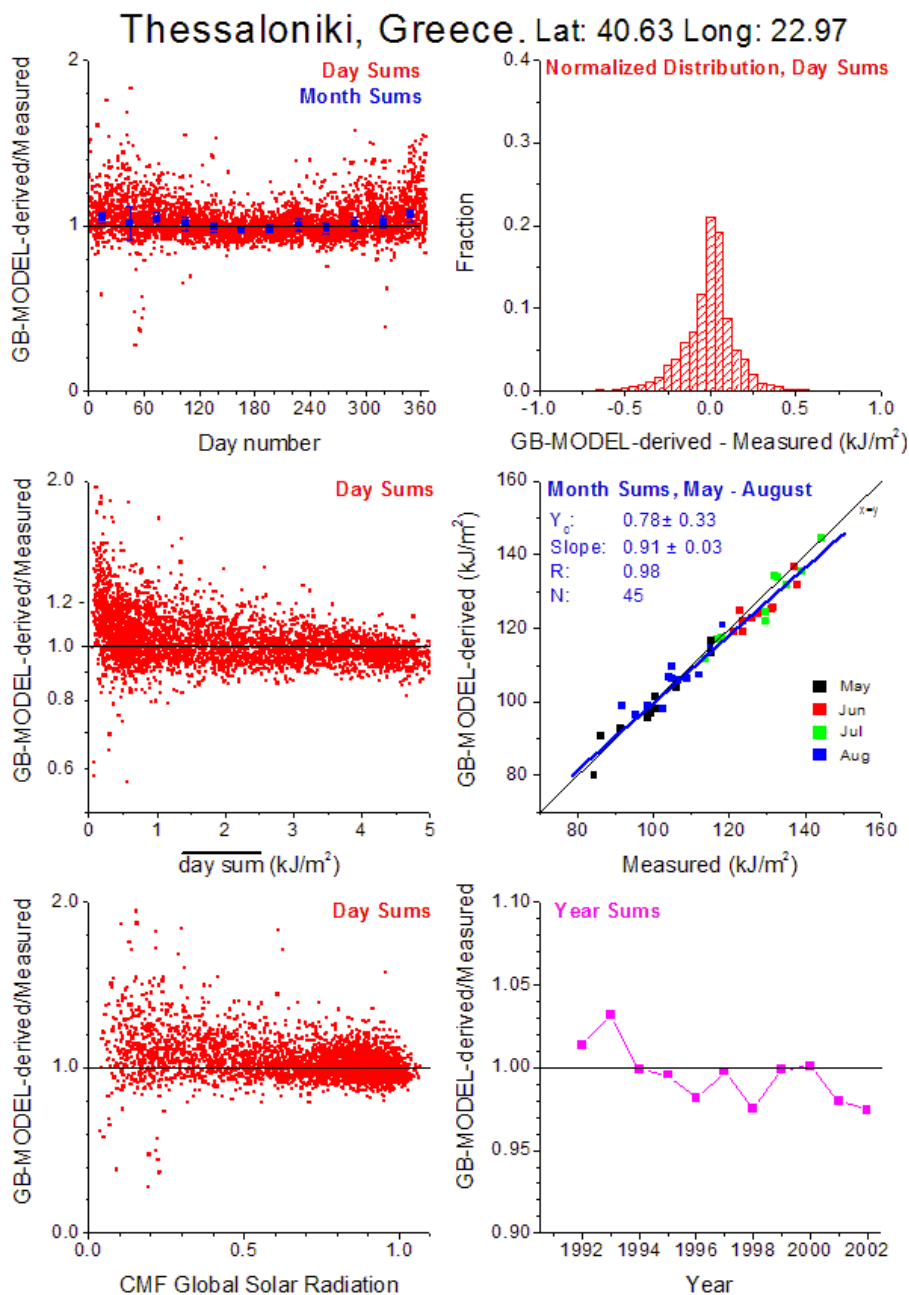
Fig. 5.1.23: Same as figure 5.1.16 for Thessaloniki, Greece.

The results of this section show that the COST 726 UV-mapping method is providing adequate results for the twelve sites especially for monthly and yearly UV-doses. The uncertainty in daily values can be up to 40–50 % under low irradiation conditions.

5.2 UNCERTAINTY DUE TO UNCERTAIN INPUT DATA

Henning Staiger [a]

a) German Meteorological Service.

The accuracy of modelled daily UV doses depends on the accuracy of the parameterisation, and on uncertainty of input used in modelling. The uncertainty due to the available input is estimated for erythemally weighted (ERY) UV, and at the wavelength 310 nm. The evaluation uses an error term in DWD's operational UV modelling algorithm. The algorithm calculates UV irradiation as a basic quantity valid for mean sea level, clear-sky conditions, and set values for aerosol properties, and for UV surface albedo. The basic quantity accounts for solar zenith angle (SZA), total ozone column (TOC), and profiles of ozone, temperature and pressure varying with season and latitude. It is adjusted by factors to current aerosol properties, albedo, altitude, and modification by clouds. These factors are constructed to be linearly independent, and thus, allow an error to be assessed representing the propagation of relative uncertainties via the individual component "i" impacting the modelled UV irradiation: uncertainty factor $= \exp(\pm\mathrm{sqrt}(\Sigma e_i^2))$, $e_i = \ln(1 + \mathrm{RMSE}_i / \mathrm{mean}_i)$. A latitudinal and seasonal dependency of inaccuracies must be assumed. The assessed uncertainty in UV due to uncertain input is valid for an individual daily UV dose derived from COST 726 fields.

The influence of uncertain TOC on the basic UV dose is estimated using the exponential proportionality for ozone-related UV changes (Madronich et al., 1998), and an appropriate radiation amplification factor, 1.10 for ERY, and 1.25 for 310 nm, respectively. In the satellite period (since 1979) the inaccuracy in TOC input for the COST 726 area is given versus ground based measurements (Bodeker et al. 2005). For the pre-satellite period it has additionally to be accounted for modelling inaccuracies (Krzyscin, 2008). According to Schwander et al. (1997) the inaccuracy in clear-sky UV modelling is less than 3 %, if monthly mean profiles are used. This coincides with the finding of den Outer et al. (2005), that the accuracy of clear-sky modelling is within ±2 % compared to measurements.

Table 5.2.1: Long-term uncertainty (RMSE$_i$ / mean$_i$) of input variables.

		35° N – 45° N	45° N – 55° N	55° N – 70° N
		10° W – 35° E	05° W – 35° E	05° E – 35° E
TOC uncertainty: Since 1979	JUL	3.16%	3.16%	3.16%
	FEB	3.16%	3.16%	3.16%
TOC uncertainty: pre-satellite:	JUL	4.49%	4.71%	5.05%
	FEB	5.86%	6.27%	6.83%
Uncertainty of AOD climatology	JUL	19.37%	24.23%	31.48%
	FEB	33.33%	41.04%	49.47%
Uncertainty of SSA at 300 nm	JUL	1.68%	1.29%	1.13%
	FEB	0.12%	1.84%	1.64%
Uncertainty in UV surface albedo	JUL	4.00%	5.35%	9.19%
	FEB	83.38%	184.18%	522.17%
Uncertainty of SOL–CMFs	JUL	14.30%	18.87%	22.59%
	FEB	27.95%	31.48%	32.99%

COST UV modelling applies a 2000 to 2008 monthly climatology of aerosol optical depth (AOD). The single scattering albedo (SSA) is set at 0.94. The impact of inaccuracy in aerosol input can be restricted to those of the climatology, because SOL–CMFs as basis of the UV–CMFs contain information on inter-diurnal variations of AOD. For the AOD climatology the relative inaccuracy is the RMSE in the individual months (Table 5.2.1). It is high in winter, because it is related to low absolute values. In the change from a low to a high turbidity atmosphere the contribution of the different aerosol optical properties to the total aerosol effect in UVB is dominated by AOD, ~55 %, and by SSA, ~30 % (Reuder

and Schwander, 1999). Hence, it has to be accounted for the inaccuracy in SSA too. Spatially covering SSA's are not available in COST 726. Alternatively, it is assumed that the inaccuracy in SSA can be estimated by the spatial variance in the Global Aerosol Data Set (Koepke et al., 1997), which is then related to the set value 0.94.

In UV, the impact of the surface albedo on the irradiation is low with the exception of snow covered surfaces. The range of inaccuracy is set at the difference between the ERA-40 derived monthly averages in case of snow and related to the mean of the snow free cases to account for inaccuracy in the ERA-40 parameterisation of water equivalent snow depths (Martin, 2004). July is free of snow, and thus, the small range of inaccuracy is taken from the inter-diurnal variations in the FMI UV surface albedo climatology (Tanskanen, 2004). The spatially high variable albedo in the Alps is not evaluated.

The inaccuracy in the SOL–CMFs is taken from the 1964 – 1993 monthly mean and accuracy (section 3.5). It is transformed to UV–CMFs applying the algorithm of den Outer et al. (2005).

Table 5.2.2 summarises the impact of uncertain input on uncertainty in individual daily UV doses for clear-sky, and all-sky conditions, respectively. The increased variability in the UV–CMFs, both spatial and temporal, dominates the impact on uncertainty for all-sky conditions. Uncertainty in ozone input has highest impact on clear-sky UV uncertainty in particular in the pre-satellite period (before 1979). High latitude winter is the exception due to the uncertain UV surface albedo. Despite the high relative variability of AOD in winter, the impact on clear-sky UV remains comparable small. The uncertainty in the UV–CMFs is slightly decreased at 310 nm compared to erythemal weighting, because of the increased diffuse irradiation at 310 nm. The exception is for high latitude winter due to high SZAs. The inaccuracy due to UV–CMFs is markedly reduced in summer compared to winter.

Table 5.2.2: Impact of uncertain input on uncertainty in individual daily erythemally weigthed (ERY), and in the daily UV doses at 310 nm, percent of mean UV dose.

| | | | 35° N – 45° N | | 45° N – 55° N | | 55° N – 70° N | |
| | | | 10° W – 35° E | | 05° W – 35° E | | 05° E – 35° E | |
			ERY	310 nm	ERY	310 nm	ERY	310 nm
clear-sky	since 1979	JUL	5.21%	5.77%	5.18%	5.50%	4.89%	5.23%
		FEB	5.33%	5.74%	7.41%	7.85%	12.95%	13.73%
	pre-satellite	JUL	6.23%	7.00%	6.51%	7.10%	6.60%	7.27%
		FEB	7.70%	8.55%	9.64%	10.54%	14.79%	15.96%
all-sky	since 1979	JUL	14.95%	12.23%	17.98%	16.74%	19.65%	19.02%
		FEB	21.97%	21.21%	22.29%	21.69%	23.64%	24.23%
	pre-satellite	JUL	15.39%	12.89%	18.48%	17.42%	20.25%	19.81%
		FEB	22.82%	22.33%	23.30%	23.00%	24.83%	25.74%

Overall, for a monthly average of an individual site the uncertainty due to uncertain input will be less than 5 %, and for 10 year monthly averages less than 1.5 %. For an individual site, it may be assumed that measured daily sums of global irradiation are available, which would reduce the uncertainty to that of clear-sky. For isolated summits the inaccuracy may increase because it could be affected by atmospheric layers below the summit, especially in case of low clouds. Moreover, the surrounding environment may show an increased variability, e.g., due to snow fields or glaciers influencing the regional albedo. There are some European sites with UV measurements showing a stronger absorbing aerosol type, e.g., Thessaloniki (Bais et al., 2005). For these sites modelled UV doses will show a higher positive bias due to a SSA set at 0.94.

5.3 COMPARISON OF UV MAPS FROM COST AND OTHER DATA SETS

Jean Verdebout [a]

a) European Commission Directorate General Joint Research Centre.

In this section, the erythemal UV maps produced by COST 726 are briefly and qualitatively compared with maps derived from METEOSAT and other data (Verdebout 2000, Arola et al. 2002, Verdebout 2004). The METEOSAT-derived maps are produced in a way very similar to the processing of COST 726 maps. The main difference resides in the cloud information used, which is derived from the visible band METEOSAT images. A parameter equivalent to the cloud optical thickness is estimated from the increase with respect to the cloudless situation of the radiance seen by METEOSAT. In this process, the presence of snow is also detected and a UV albedo inferred. This is done at the full spatial resolution of METEOSAT (~4 km in central Europe). The cloud parameter and the UV albedo are then re-sampled on a regular $0.05° \times 0.05°$ grid and used as input into a Look Up Table to produce the surface erythemal down welling irradiance. Several images per day are used to reconstruct daily dose maps. The ozone data come from TOMS ($1° \times 1.25°$), the aerosol are taken into account by gridding daily horizontal visibility measurements from ~1000 ground stations and the altitude is from the GOTO30 data set, as for COST 726 maps. The period covered by these METEOSAT-derived maps is from January 1st 1984 to August 31st 2003.
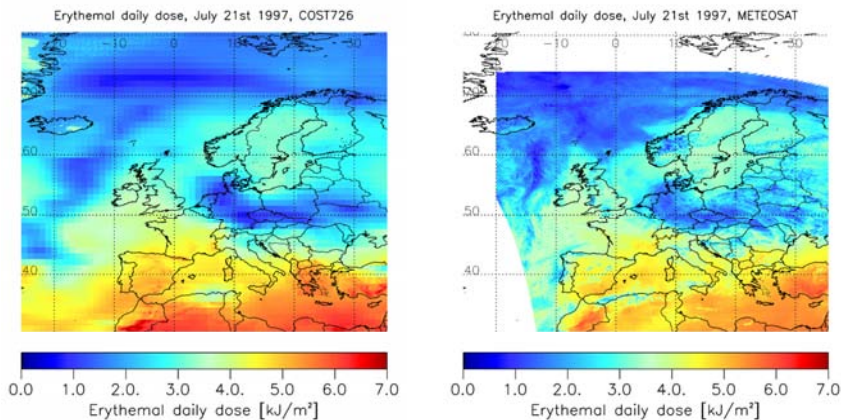

Fig. 5.3.1: Erythemal daily dose maps on July 1st 1997, COST 726 (left) and METEOSAT-derived (right).

Figure 5.3.1 shows the erythemal daily dose on July 21st 1997. It can be seen that, with respect to the METEOSAT-derived the values in the COST map are higher in the south. However, the spatial patterns and in particular those associated with clouds match fairly well. This means that, despite their lower intrinsic spatial resolution, the COST maps do document the overall distribution of the UV radiation on a single day.

Figure 5.3.2 shows the difference with respect to multi-year averages (see section 6.2) of the monthly averaged daily erythemal dose in April 1984 and in June 1991. Again the spatial patterns match reasonably well. In this case, a quantitative judgment is not really possible because the period for defining the multi-year average is different for the two data sets. In June 1984, the excess over France and southern England correspond to low ozone and low cloudiness while the deficit over Greece and Turkey is caused by high ozone and heavy cloudiness. In June 1991, the pronounced deficit over Scandinavia and Finland mostly corresponds to heavy cloudiness, the ozone being quite regular from year to year in this month.
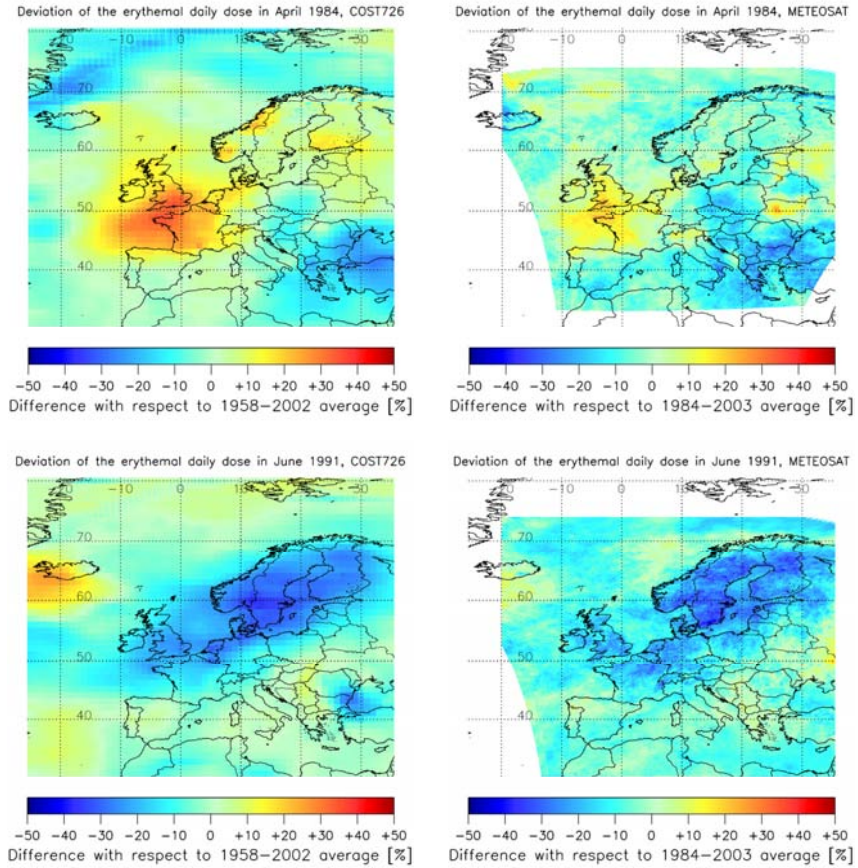
Fig. 5.3.2: Difference with respect to the multi-year averages of the monthly averaged erythemal daily dose in April 1984 (top) and June 1991 (bottom), COST 726 (left) and METEOSAT-derived (right).

6   RESULTS: UV RADIATION IN THE PAST

Jean Verdebout [a], Peter N. den Outer [b], Janusz Krzyścin [c], Alois Schmalwieser [d].

a) European Commission Directorate General Joint Research Centre; b) Dutch National Institute for Public Health and the Environment (RIVM); c) Polish Academy of Sciences, Institute of Geophysics; d) Institute of Medical Physics and Biostatistics, University of Veterinary Medicine, Austria.

Long-term assessment of the European UV-climate relevant for biological effects cannot be directly based on ground-based measurements of UV, because such measurements are not available at a sufficient number of locations and for the required long time periods. Therefore, modelling approaches are required to analyse the past UV-climate in relation to ozone, clouds and aerosols. The previous chapter provides an extensive validation of two such approaches, and in this chapter these approaches are used to analyse the past UV-climate. The approaches were a selected subset of methods that were included in a modelling exercise carried out by COST action 726. The modelling exercise demonstrated that several methods are capable of providing accurate UV-estimates, provided that the model-input data is of sufficient quality, i.e. data on ozone column, global radiation (cloud-effects) and aerosols. In section 6.1 the UV-climate is reconstructed for 8 locations using ground-based measurements and also compared with time series extracted from the COST 726 UV-maps. Section 6.2 illustrates the map data set produced by COST 726. In section 6.3 a wavelet analysis is made, identifying different time scales in the UV changes. In the last section results of a questionnaire regarding the use of photobiological weighting functions, action spectra, are presented and the influence of spectral resolution, inter and extrapolation of these action spectra of the derived effective UV is discussed.

6.1 STATION RESULTS ERYTHEMAL WEIGHTED UV

Peter N. den Outer [a], Harry Slaper [a], Jean Verdebout [b].

a) Dutch National Institute for Public Health and the Environment (RIVM); b) European Commission Directorate General Joint Research Centre.

Within this COST action 726, a modelling exercise has been carried out, where 16 different reconstruction models were tested against ground-based UV-measurements (Koepke et al., 2008). A number of models were found to have results that were in good agreement with the measurements, both in absolute and relative comparisons. We use one of those models to make an analysis of the UV radiation levels over the European Continent in the past 25–40 years using COST 726 and SCOUT-O3 datasets. The latter data sets contain ground-based ozone and pyranometer measurements accompanied with snow cover and aerosol climatology (section 3.2). These data sets were gathered within the European project SCOUT-O3. Now we present results for 8 sites covering 40–67 ° N.

This reconstruction model, which was developed at RIVM, is described by Den Outer et al. (2005). It combines effective UV-dose rates taken from a look-up table (UV as a function of ozone and SZA) pre-calculated using the TUV-model with a standard cloud-free atmosphere (Madronich et al., 1998). The RIVM-model makes use of site information of the ground-albedo and (monthly) aerosol climatology. CMFs for the UV daily sums are derived from the pyranometer measurements using an SZA-dependent empirical relationship (den Outer et al., 2005). It is the same relationship that has been used to derive CMFs for the UV maps from the corrected ERA-40 dataset. The relationship between the SOL–CMFs and UV–CMFs was initially established at Bilthoven.

The yearly erythemally weighted UV sums are shown as a function of time for the eight sites in figure 6.1.1 for the eight sites. We also show the yearly sums constructed from the time series that have been extracted from the COST 726 UV maps. The yearly sums range from 290 ± 22 kJ/m^2 for Sodankylä at $67 ° N$ to 720 ± 44 kJ/m^2 for Thessaloniki at $40 ° N$, based on ground-based modelling. A severe overestimation by the UV map-extracted yearly sums occurs for Thessaloniki in this respect; for the UV-map-extracted result we find 792 ± 50 kJ/m^2, see also table 6.1.1. This can most likely be attributed to the heavy aerosol loading for Thessaloniki, which is not fully grasped by the aerosol climatology as included

in the COST 726 mapping method. The overall year-to-year variability does not show a distinct behaviour for one of the sites, but ranges from 6 to 8 %. The variability of the monthly UV sum (from year-to-year) was lowest at Thessaloniki during the summer months as may be expected from the usual absence of clouds (see Fig. 6.1.2). The relative variation is of the order of 5–6 % for these months while the rest of the sites show an almost season independent variability of 10–17 %.
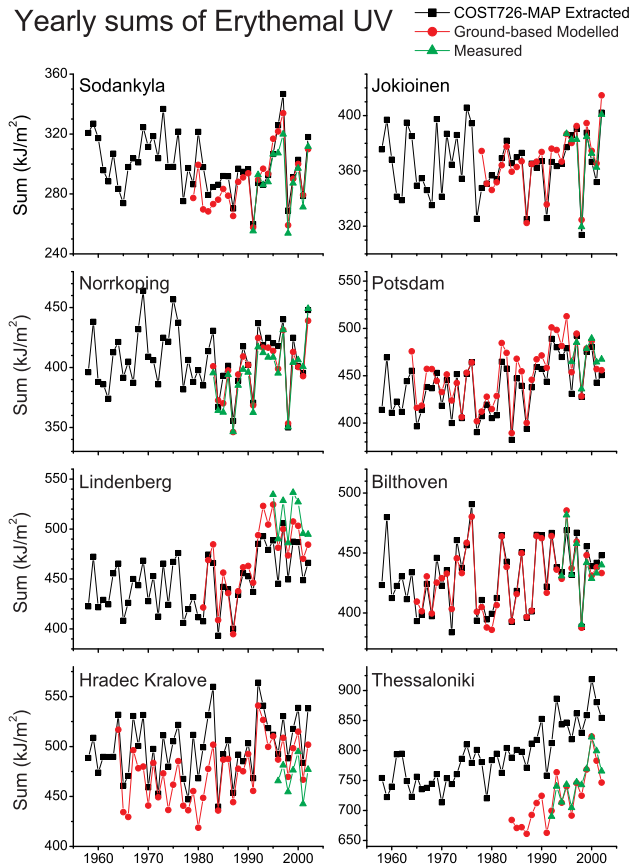

Fig. 6.1.1: Evolution of the yearly erythemally weighted UV sum for eight European sites. Different colours indicate underlying data used.

Table 6.1.1: Derived yearly sums and variability for eight European locations using ground-based modelling (GB) or the COST 726 UV-maps extracted time series (COST).

Code	Site	Lat. (deg. dec)	Yearly sum (kJ/m^2) GB	COST	% Variability GB	COST
FIS	Sodankylä	67.36	288.1	294.3	6.7	6.5
FIJ	Jokioinen	60.81	366.8	363.4	5.7	5.6
SEN	Norrköping	58.58	398.1	405.3	6.3	6.9
DEP	Potsdam	52.36	451.0	440.0	6.8	6.7
DEL	Lindenberg	52.21	470.3	456.3	7.5	6.7
NLB	Bilthoven	52.12	428.6	430.4	6.3	6.7
CRH	Hradec Kralove	50.18	475.0	500.1	6.3	6.3
GRT	Thessaloniki	40.63	720.0	832.2	6.2	4.9
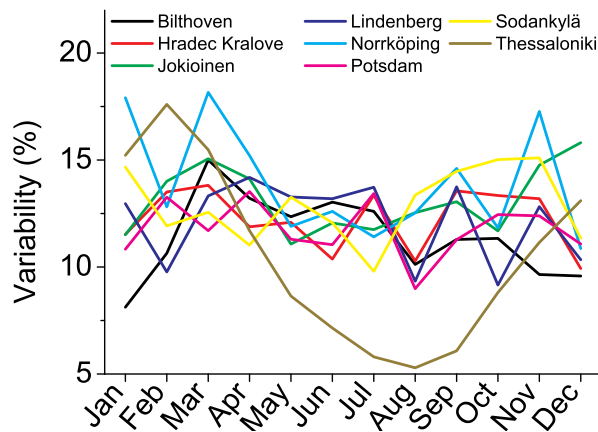
Fig. 6.1.2: Variability of the monthly erythemally weighted UV sum, using the modelled data based on ozone and pyranometer measurements. The whole available period is included.

Binning the reconstructed UV dose per decades, we derive the relative long-term changes as given in figure 6.1.3. Time window is limited to the period where both ozone and pyranometer data is available. The same type of graph is made for the clear-sky situation, and shown as figure 6.1.4. Prior to 1980 the average yearly UV sums appear to be on a stable level. An increase is seen for all sites after the eighties. Characterizing this increase by a single linear trend line yields 0.45 ± 0.05 % per year for the cloudy sky situations and 0.22 ± 0.4 % per year for the clear-sky situation. A similar behaviour is found for a number of other sites where the COST 726 ozone and COST 726 CMFs have been implemented (see Fig. 6.1.5). Additionally, a trend in the aerosol optical depth has been identified at Thessaloniki (Kazadzis et al., 2007). The result of this trend being a larger increase of the annual UV sum 14 % per decade for the all-sky situations and 10 % for the clear-sky estimates, than without this aerosol trend in that case 3 and 8 % increases per decade are found, for all- and clear-sky situations respectively. The fact that for the cloudy UV dose, a significantly larger trend is shown, compared with the clear-sky UV, suggests that part of the UV increase must be induced by a diminishing of cloud impact on the UV irradiance. In figure 6.1.6 we show the CMFs on the yearly sums as a function of the year; the cloudy sky yearly sum is divided by the corresponding clear sky yearly sum. The overall cloud impact on yearly UV is the largest in The Netherlands (CMF = 0.66), and the smallest in Greece (CMF = 0.81). But more interestingly, all sites show a diminishing of the cloud impact for years after 1979. The CMF increases with 0.020 ± 0.008 per

decade. If this can be regarded as a genuine trend in cloudiness is still to be investigated, because the number of years included in the analysis is too small.
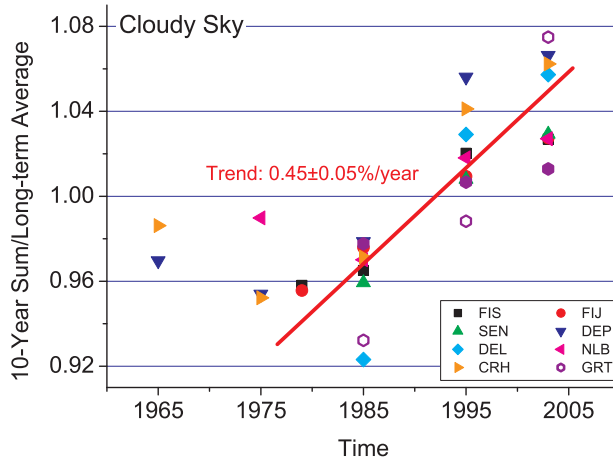

Fig. 6.1.3: Reconstructed yearly UV-sums averaged per decade using ground-based measured ozone and pyranometer data. FIS and FIJ have only one year sum for 1960–1979, i.e. 1979. The solid points for GRT are derived using constant aerosol climatology.
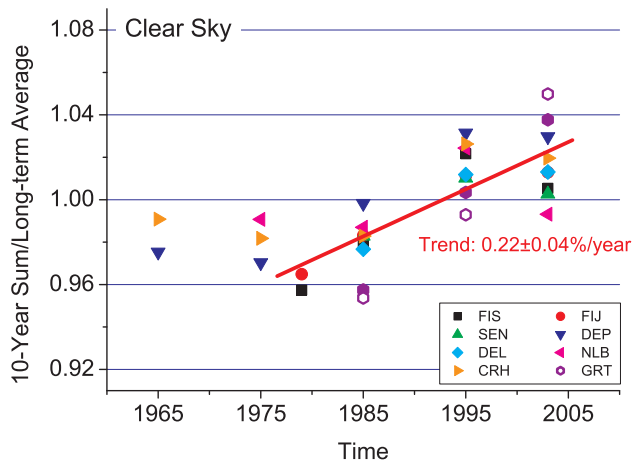

Fig. 6.1.4: Reconstructed yearly UV-sums averaged per decade using ground-based measured ozone. FIS and FIJ have only one year sum for 1960-1979, i.e. 1979. The solid points for GRT are derived using constant aerosol climatology.
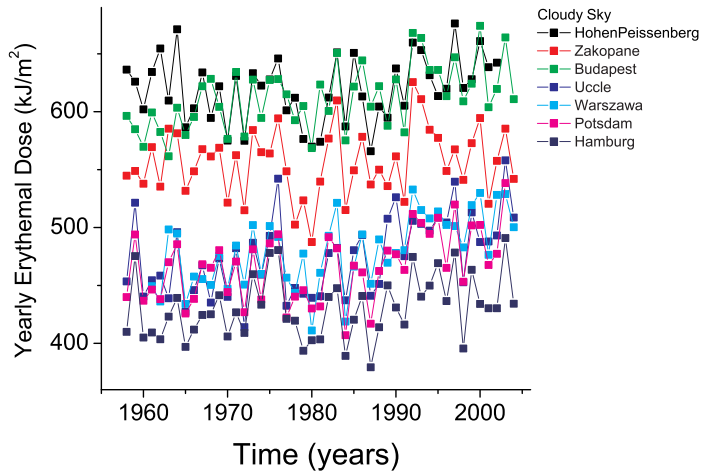
Fig. 6.1.5: Reconstructed yearly UV-sums for some Central European sites, using COST 726 ozone and CMF.
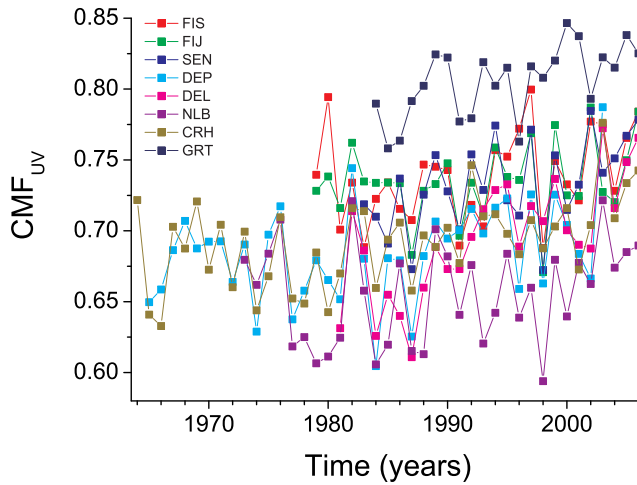

Fig. 6.1.6: Derived annual cloud impact on the yearly UV sums, expressed as yearly CMF, as function of the year for the eight European sites.

6.2 MAPS – ERYTHEMAL WEIGHTED UV

Jean Verdebout [a], Henning Staiger [b], Peter N. den Outer [c], Natalia Chubarova [d].

a) European Commission Directorate General Joint Research Centre; b) German Meteorological Service; c) Dutch National Institute for Public Health and the Environment (RIVM); d) Moscow State University, Meteorological Observatory.

The purpose of this section is to illustrate the map data set produced by COST 726. As stated before, the maps cover the area from 25.5° W to 35.5° E and 30.5 to 80.5° N with a spatial resolution of 0.05°. The basic product is made of daily dose maps with the spectral weighting corresponding to the erythemal effect and at 7 discrete wavelengths (295, 300, 305, 310, 315, 330 and 360 nm) with a 5 nm FWHM triangular slit function. This set of 8 maps has been produced for each day in the period from January 1st 1958 to August 31st 2002. Thanks to the completeness of the input data sets, there is not any missing day.
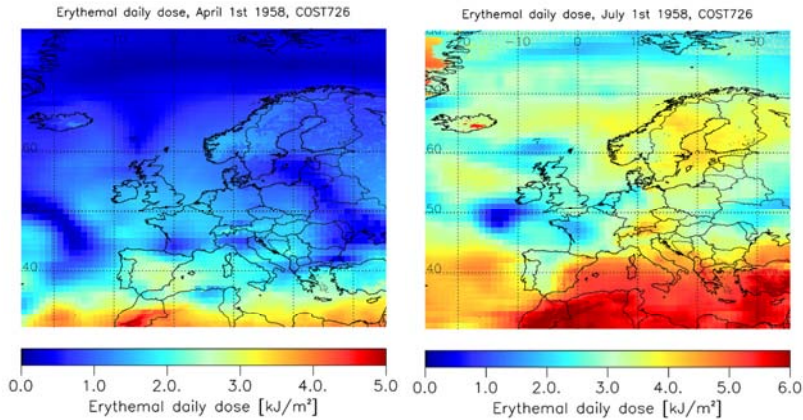

Fig. 6.2.1: Two examples of erythemal daily dose maps, respectively on April 1st 1958 and July 1st 1958.

The daily dose maps are illustrated for two days in figure 6.2.1. In addition to the latitude gradient associated with the solar zenith angle, one can distinguish patterns caused by cloudiness, snow cover and altitude. In order to document the year to year variability and to make visible systematic geographical patterns, it is useful to generate monthly averaged values (Fig. 6.2.2) and multi-year (1958–2002) averages of the monthly averaged values (Fig. 6.2.3). In these averaged maps, the cloud patterns are smoothed out but the attenuation by clouds is present.
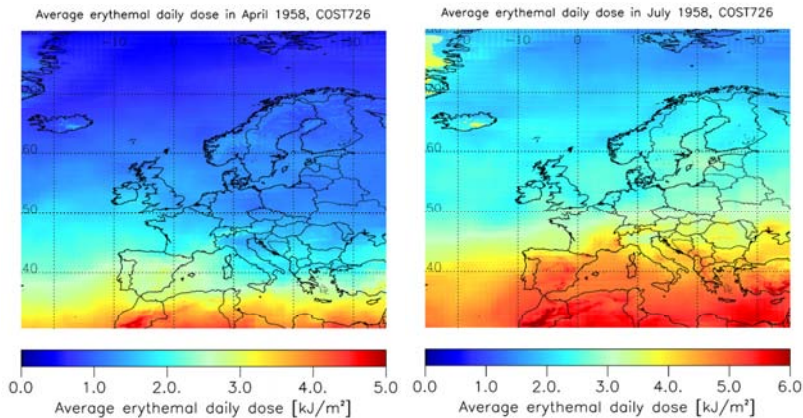

Fig. 6.2.2: Two examples of monthly averaged erythemal daily dose maps, respectively in April and July 1958.
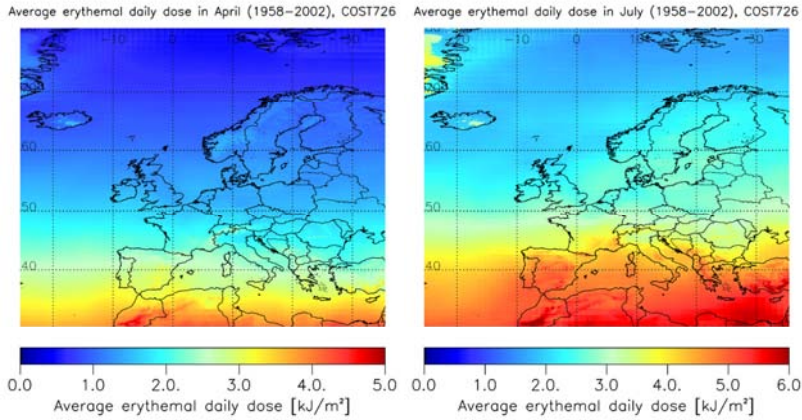
Fig. 6.2.3: Multi-year averages of monthly averaged erythemal daily dose maps for April and July.

The multi-year averages allow distinguishing systematic geographical differences. However, because of the limitations of a representation with a colour table, it is necessary to zoom in and to use an optimized scale. Figure 6.2.4 shows the multi-year average (erythemal radiation) over the Alpine arc and a large part of Italy in April (left) and in August (right). The UV radiation enhancement over the mountains is more pronounced in spring when it is caused both by the altitude and the presence of snow, in August only the altitude effect is present (except over permanent glaciers). One can also notice a lower UV intensity in the Po valley with respect to the same latitude in the Rhone valley. This feature is caused by a heavier cloudiness and larger aerosol load in Northern Italy.
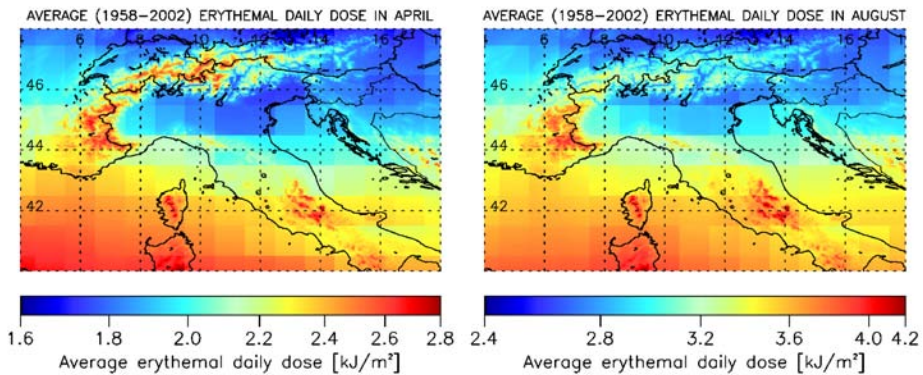

Fig. 6.2.4: Multi-year averages of the monthly averaged erythemal daily dose for April and August, over the alpine arc and a large part of Italy.

Figure 6.2.5 shows the multi-year average in the northern part of Norway, Sweden and Finland in March. Again, the effects of altitude and snow cover are visible, including over the Gulf of Bothnia, which is regularly ice covered at that time of the year. Figure 6.2.6 shows how the Cantabric Mountain system acts as a climatological barrier with a noticeably heavier cloudiness north of the range.
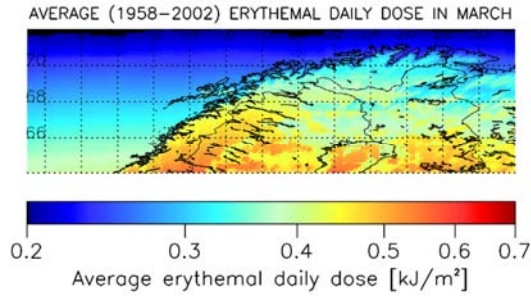
AVERAGE (1958–2002) ERYTHEMAL DAILY DOSE IN MARCH

Average erythemal daily dose [kJ/m²]

Fig. 6.2.5: Multi-year averages of the monthly averaged erythemal daily dose for March, over northern Norway, Sweden and Finland.

AVERAGE (1958–2002) ERYTHEMAL DAILY DOSE IN MAY
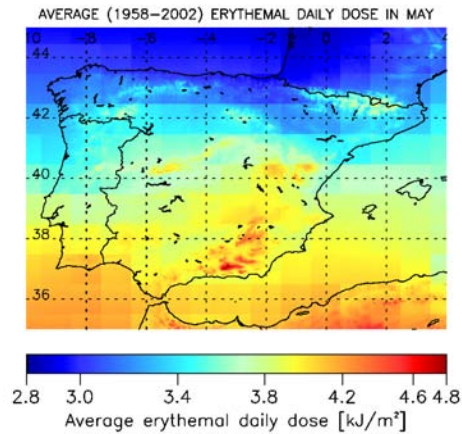

Average erythemal daily dose [kJ/m²]

Fig. 6.2.6: Multi-year averages of the monthly averaged erythemal daily dose for May, over the Iberian Peninsula.

The main interest of the COST 726 map data set is probably to document the variability in time of the surface UV radiation. Again because of the dominant latitude gradient and the limitations of the representation by means of a colour table, it is not easy to distinguish the differences between for instance the images of figure 6.2.2 (monthly averages in 1958) and those of figure 6.2.3 (multi-year averages). Instead, figures 6.2.8 to 6.2.19 show, for each month and each year, the relative difference between the monthly averaged erythemal daily dose and its corresponding multi-year average (for the same month); the multi-year averages maps themselves are illustrated in figure 6.2.7. It then appears that the year to year variability is large, easily reaching ±50 % in spring. The two main factors responsible for this variability are cloudiness and total column ozone. All possible combinations can be found, i.e. cloudiness and ozone sometimes add their effect to produce a pronounced excess or deficit or compensate each other. The variability is less in summer because the atmospheric ozone is more regular in this season.

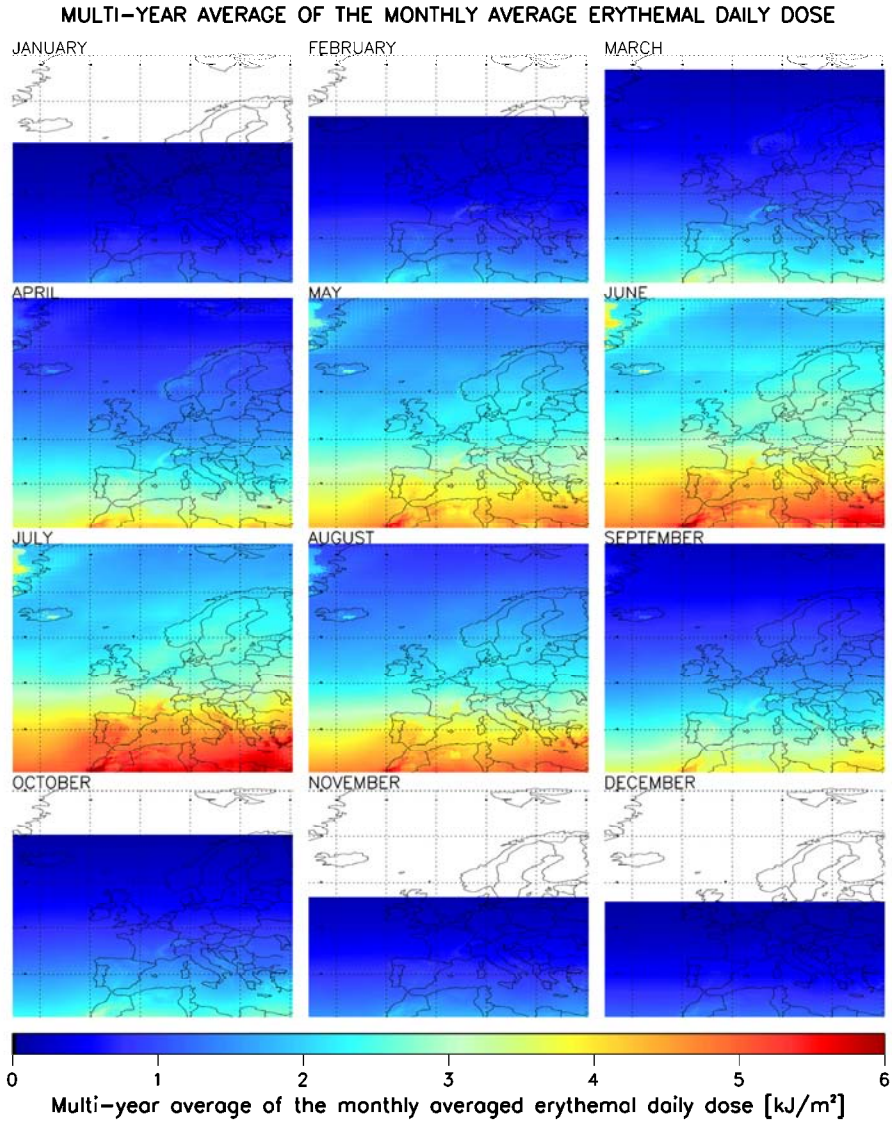**Fig. 6.2.7**: Multi-year averages (Jan.-Aug.: 1958-2002, Sep.-Dec.: 1958-2001) of the monthly averaged erythemal daily dose over Europe.

DEVIATION OF THE MONTHLY AVERAGED ERYTHEMAL DAILY DOSE
WITH RESPECT TO THE 1958-2002 MEAN (JANUARY)

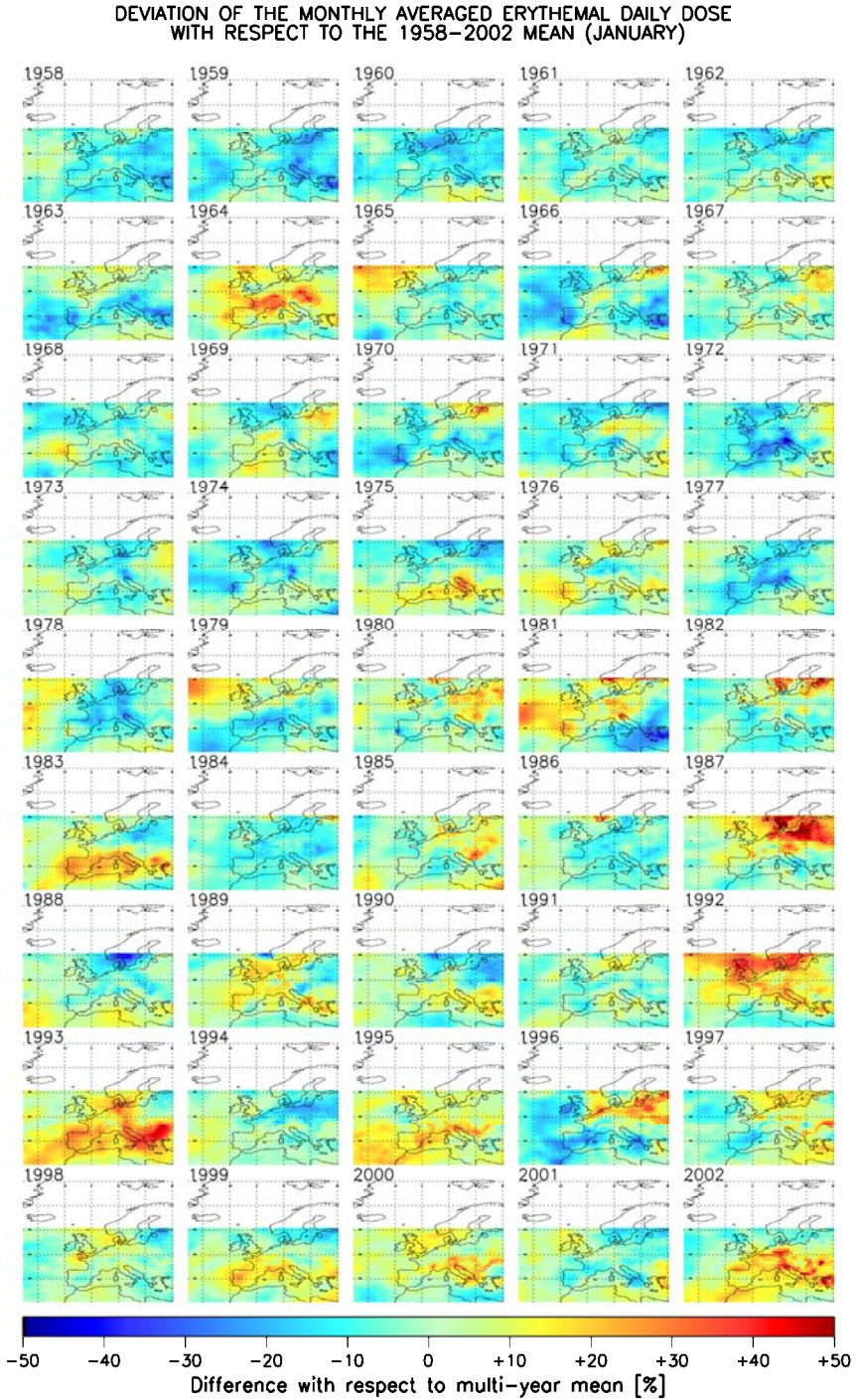

Difference with respect to multi-year mean [%]

Fig. 6.2.8: Year to year variability of the monthly averaged erythemal daily dose in January.

Fig. 6.2.9: Year to year variability of the monthly averaged erythemal daily dose in February.

DEVIATION OF THE MONTHLY AVERAGED ERYTHEMAL DAILY DOSE
WITH RESPECT TO THE 1958–2002 MEAN (MARCH)

Fig. 6.2.10: Year to year variability of the monthly averaged erythemal daily dose in March.

DEVIATION OF THE MONTHLY AVERAGED ERYTHEMAL DAILY DOSE
WITH RESPECT TO THE 1958-2002 MEAN (APRIL)

Fig. 6.2.11: Year to year variability of the monthly averaged erythemal daily dose in April.

DEVIATION OF THE MONTHLY AVERAGED ERYTHEMAL DAILY DOSE
WITH RESPECT TO THE 1958-2002 MEAN (MAY)
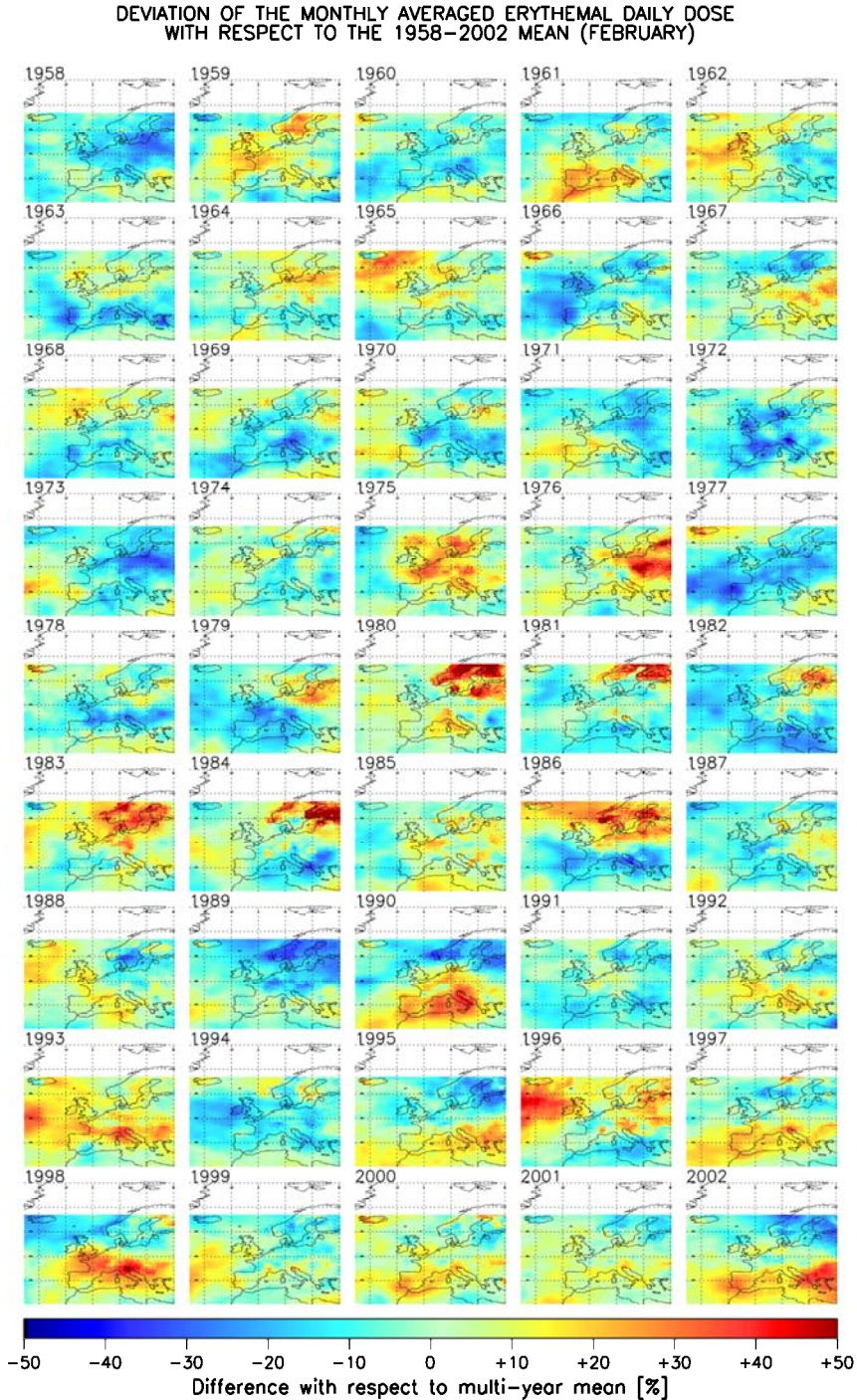

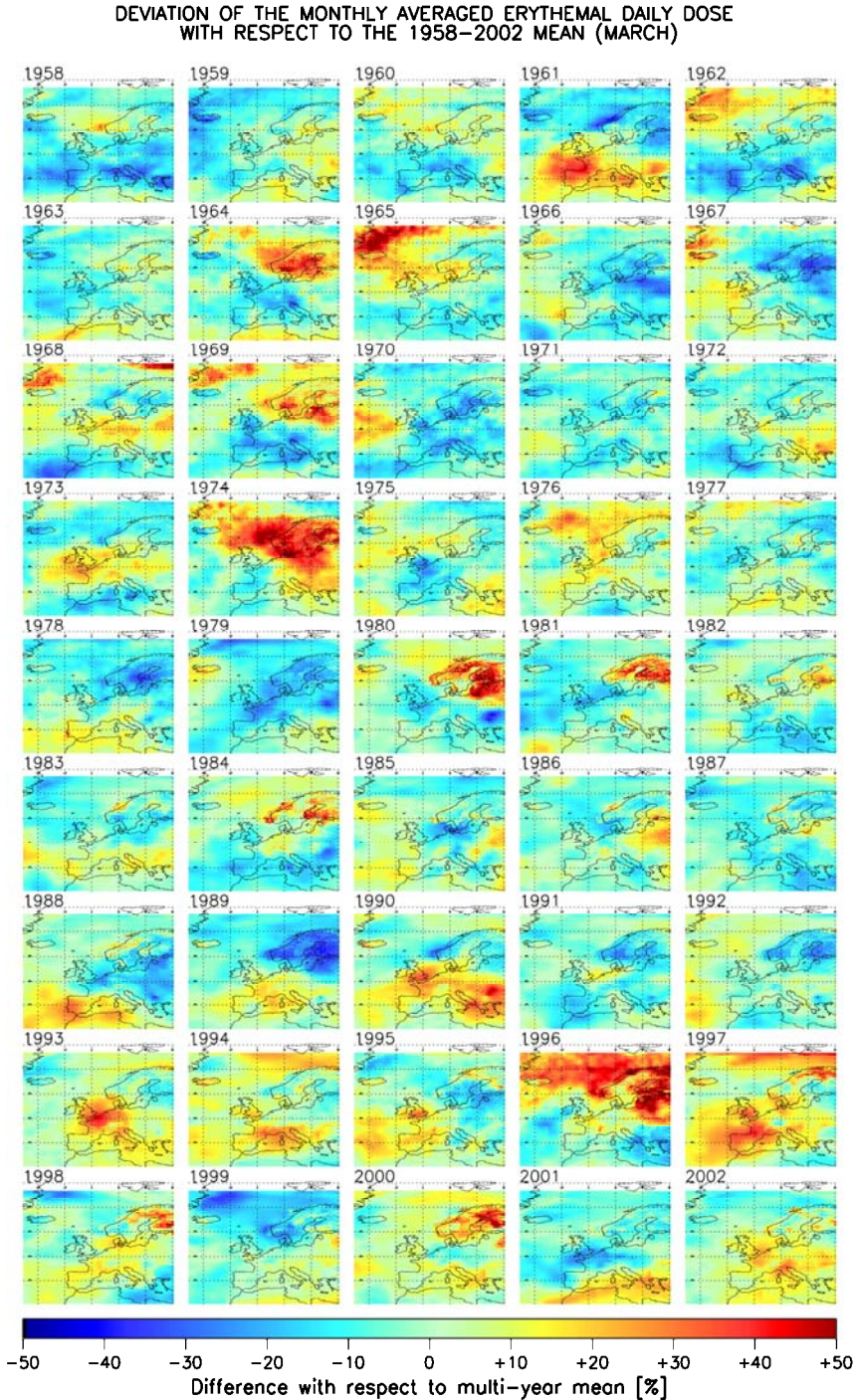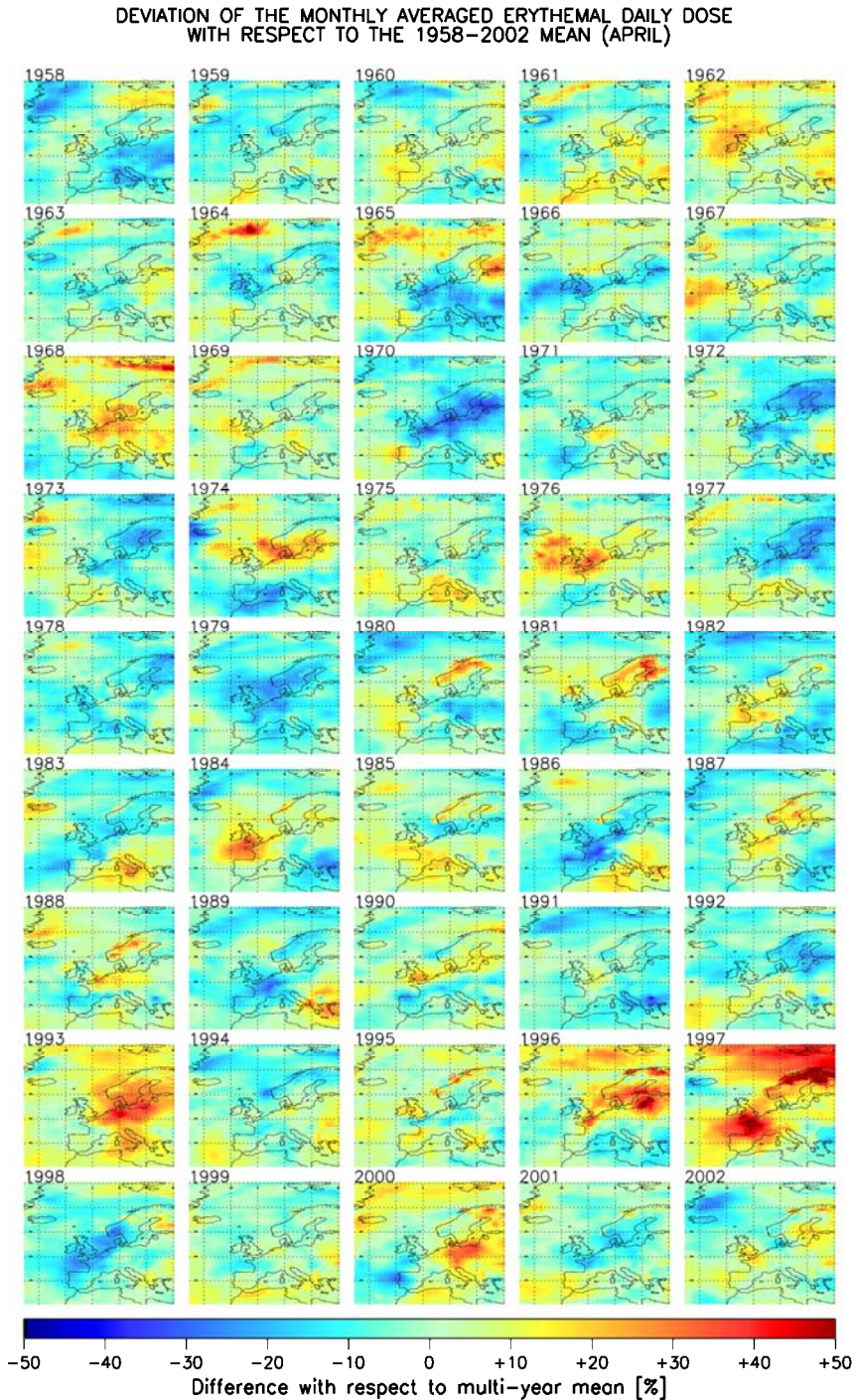Difference with respect to multi-year mean [%]
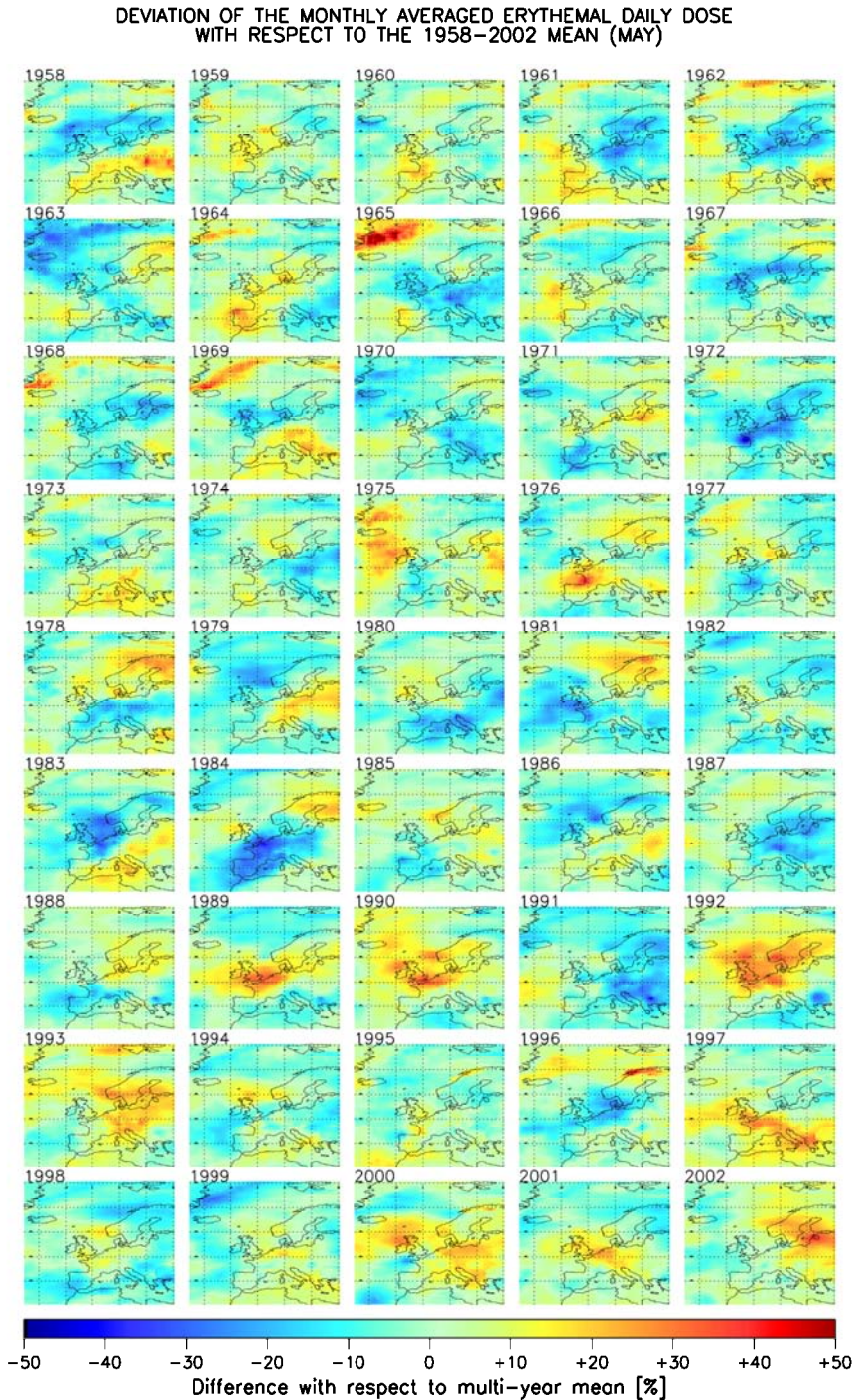
Fig. 6.2.12: Year to year variability of the monthly averaged erythemal daily dose in May.
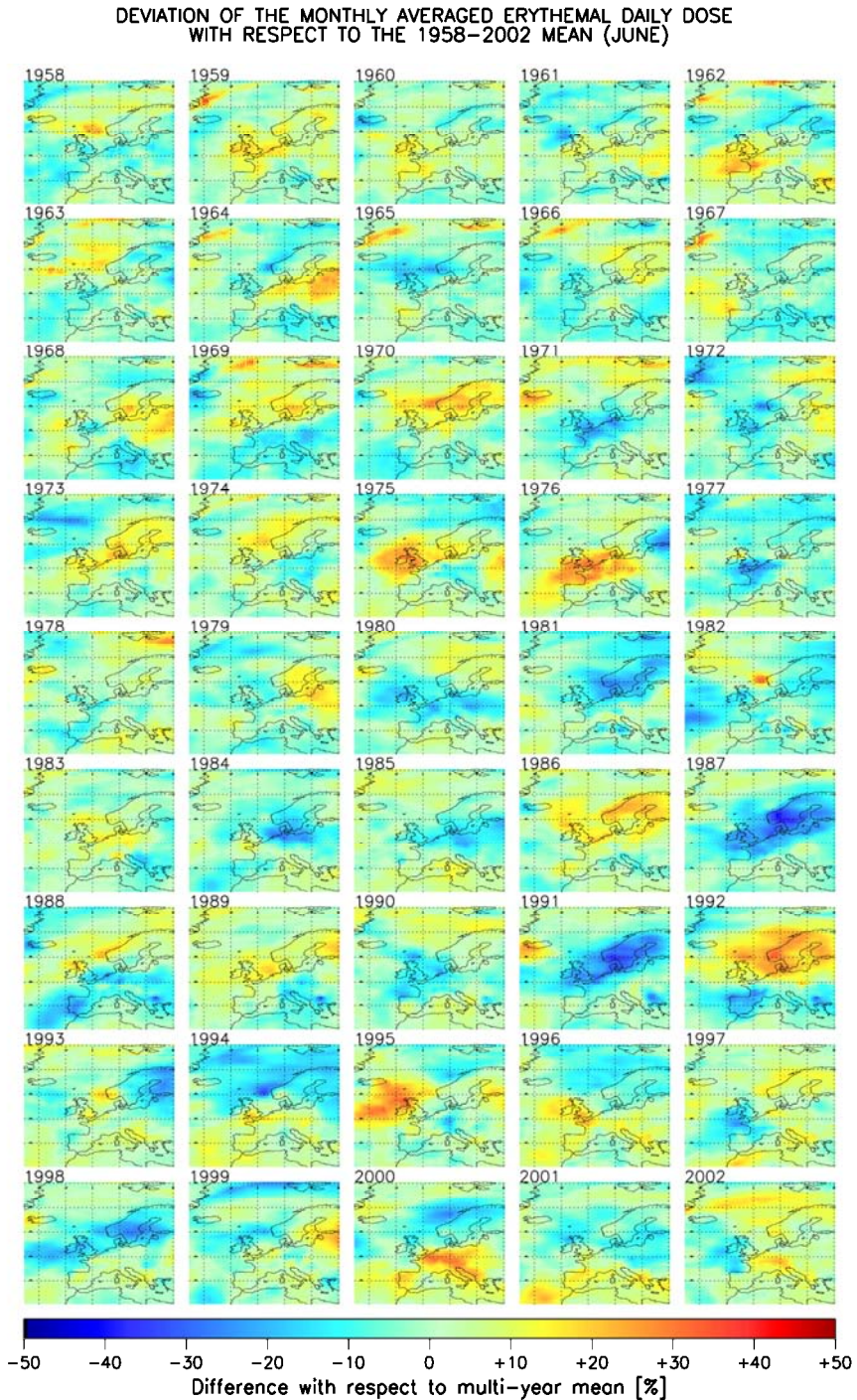
Fig. 6.2.13: Year to year variability of the monthly averaged erythemal daily dose in June.

DEVIATION OF THE MONTHLY AVERAGED ERYTHEMAL DAILY DOSE
WITH RESPECT TO THE 1958-2002 MEAN (JULY)

Fig. 6.2.14: Year to year variability of the monthly averaged erythemal daily dose in July.

DEVIATION OF THE MONTHLY AVERAGED ERYTHEMAL DAILY DOSE
WITH RESPECT TO THE 1958–2002 MEAN (AUGUST)

Fig. 6.2.15: Year to year variability of the monthly averaged erythemal daily dose in August.

DEVIATION OF THE MONTHLY AVERAGED ERYTHEMAL DAILY DOSE
WITH RESPECT TO THE 1958-2001 MEAN (SEPTEMBER)

Fig. 6.2.16: Year to year variability of the monthly averaged erythemal daily dose in September.

DEVIATION OF THE MONTHLY AVERAGED ERYTHEMAL DAILY DOSE
WITH RESPECT TO THE 1958-2001 MEAN (OCTOBER)

Difference with respect to multi-year mean [%]

Fig. 6.2.17: Year to year variability of the monthly averaged erythemal daily dose in October.

DEVIATION OF THE MONTHLY AVERAGED ERYTHEMAL DAILY DOSE
WITH RESPECT TO THE 1958-2001 MEAN (NOVEMBER)

Difference with respect to multi-year mean [%]

Fig. 6.2.18: Year to year variability of the monthly averaged erythemal daily dose in November.

Fig. 6.2.19: Year to year variability of the monthly averaged erythemal daily dose in December.
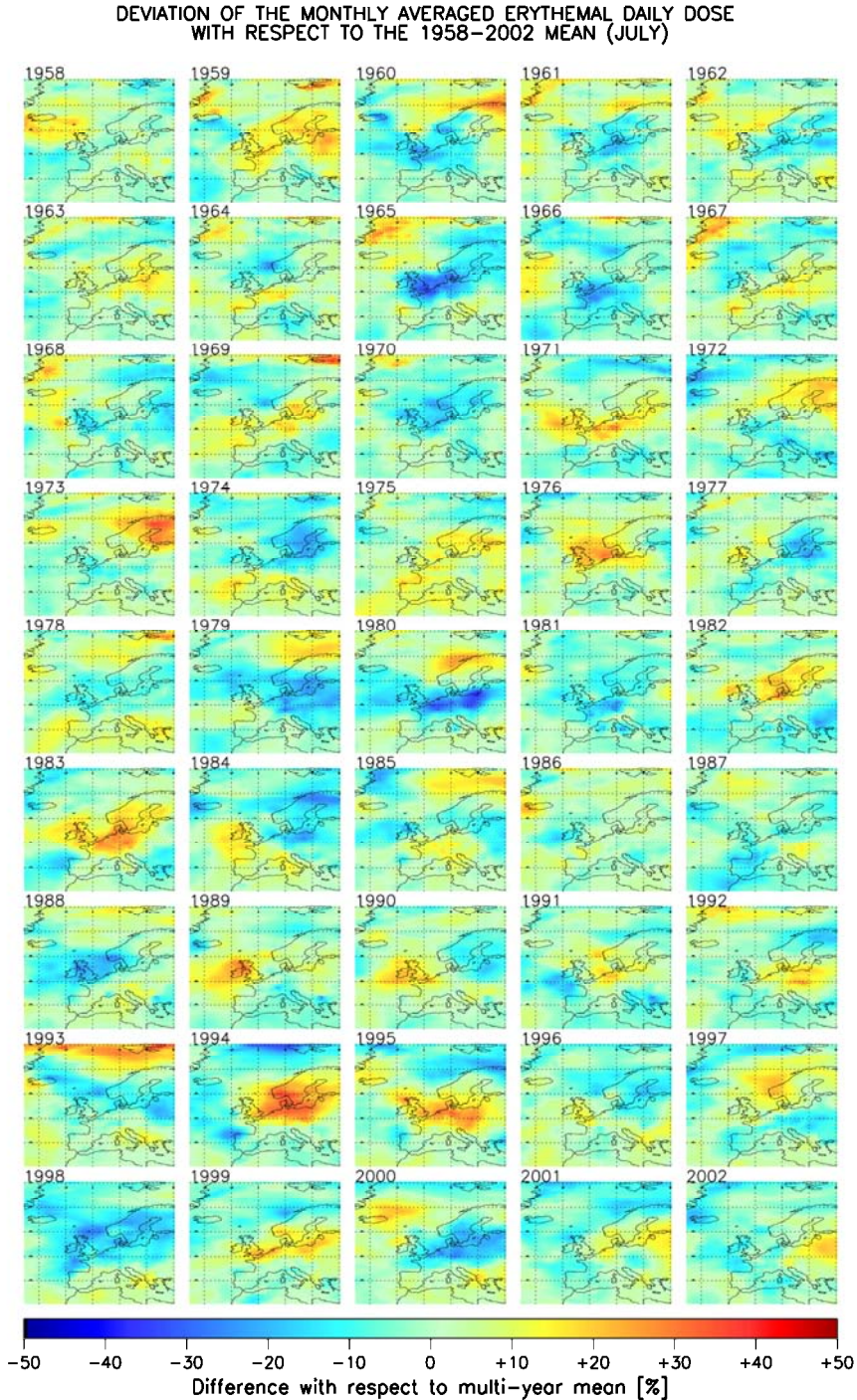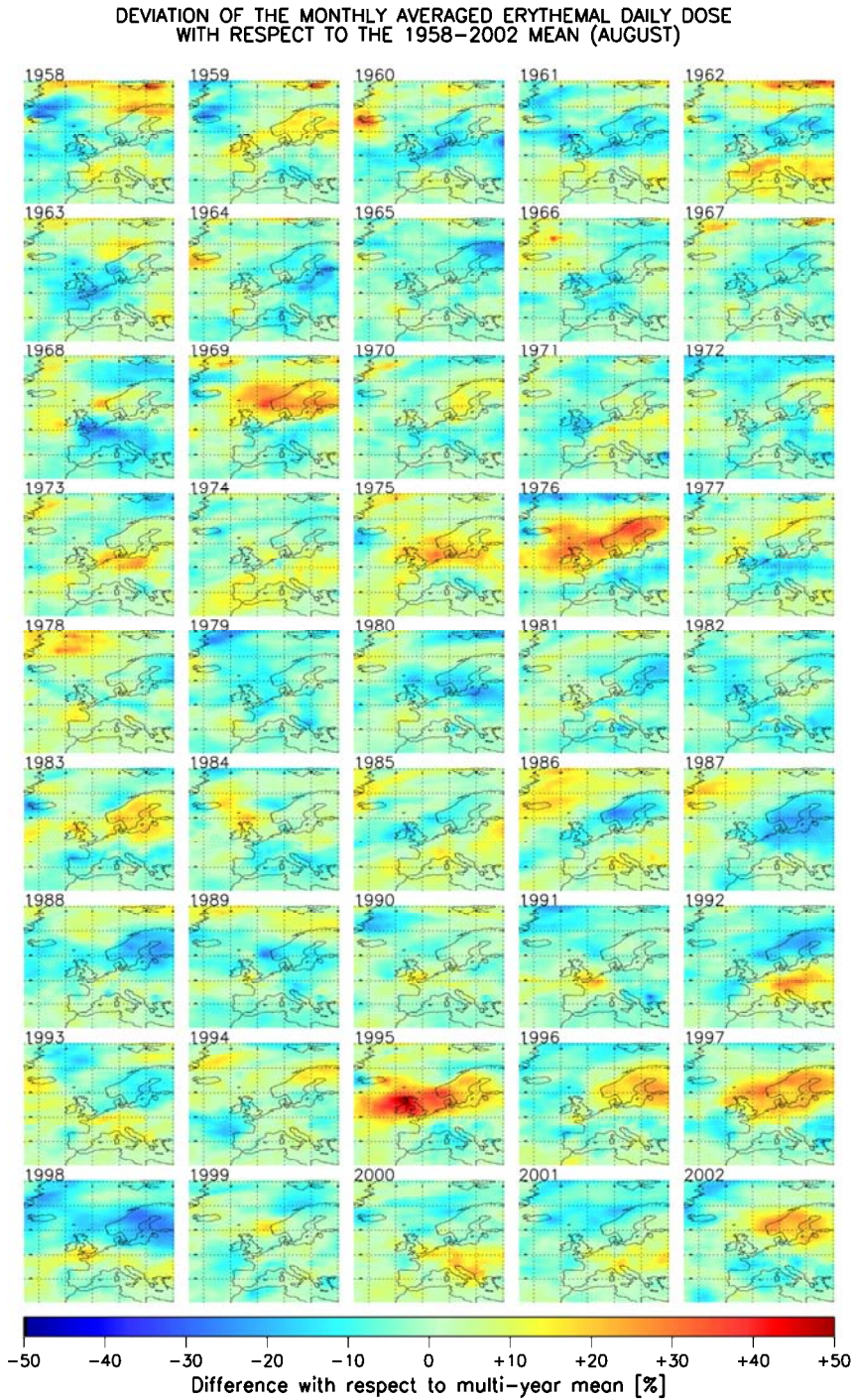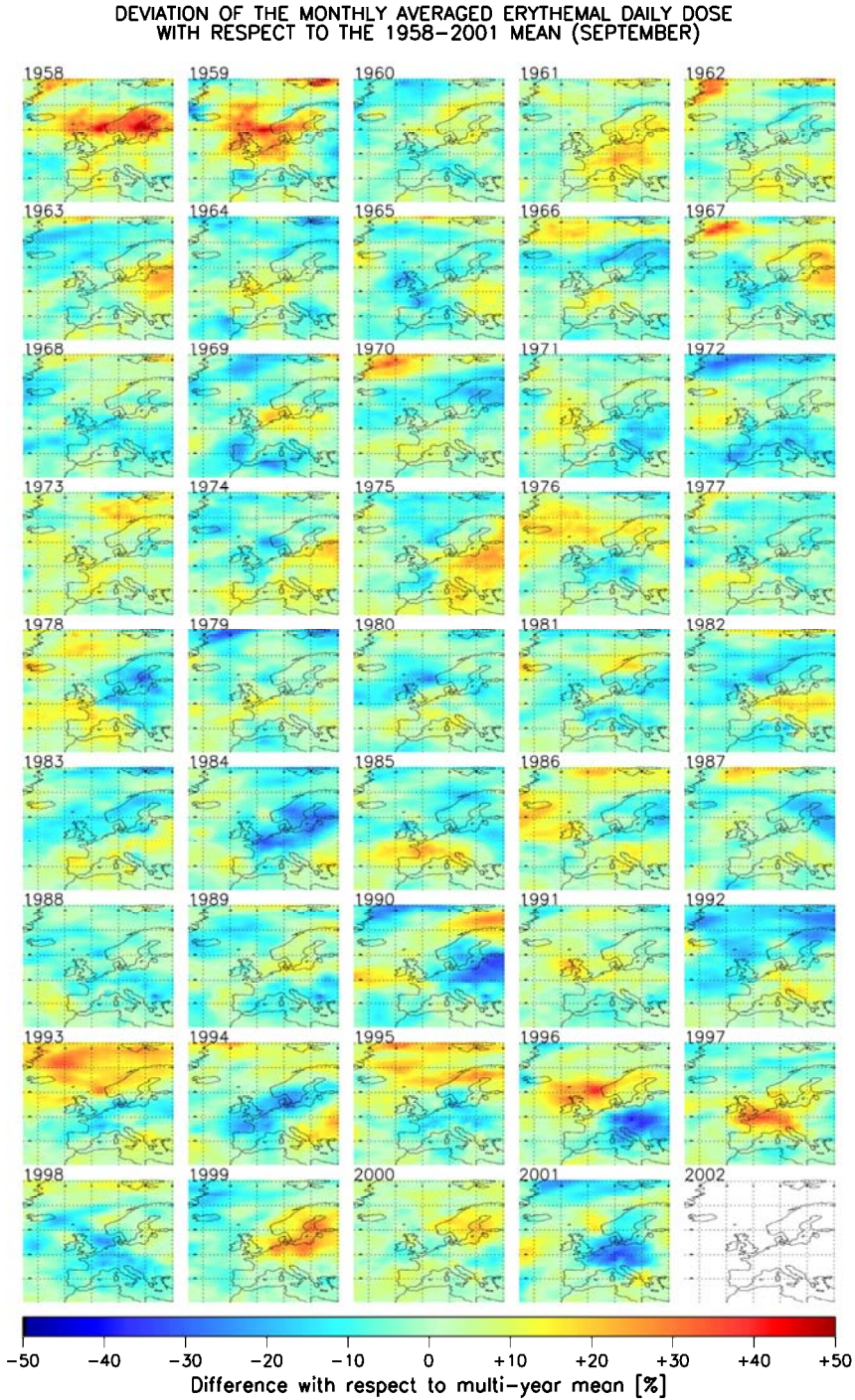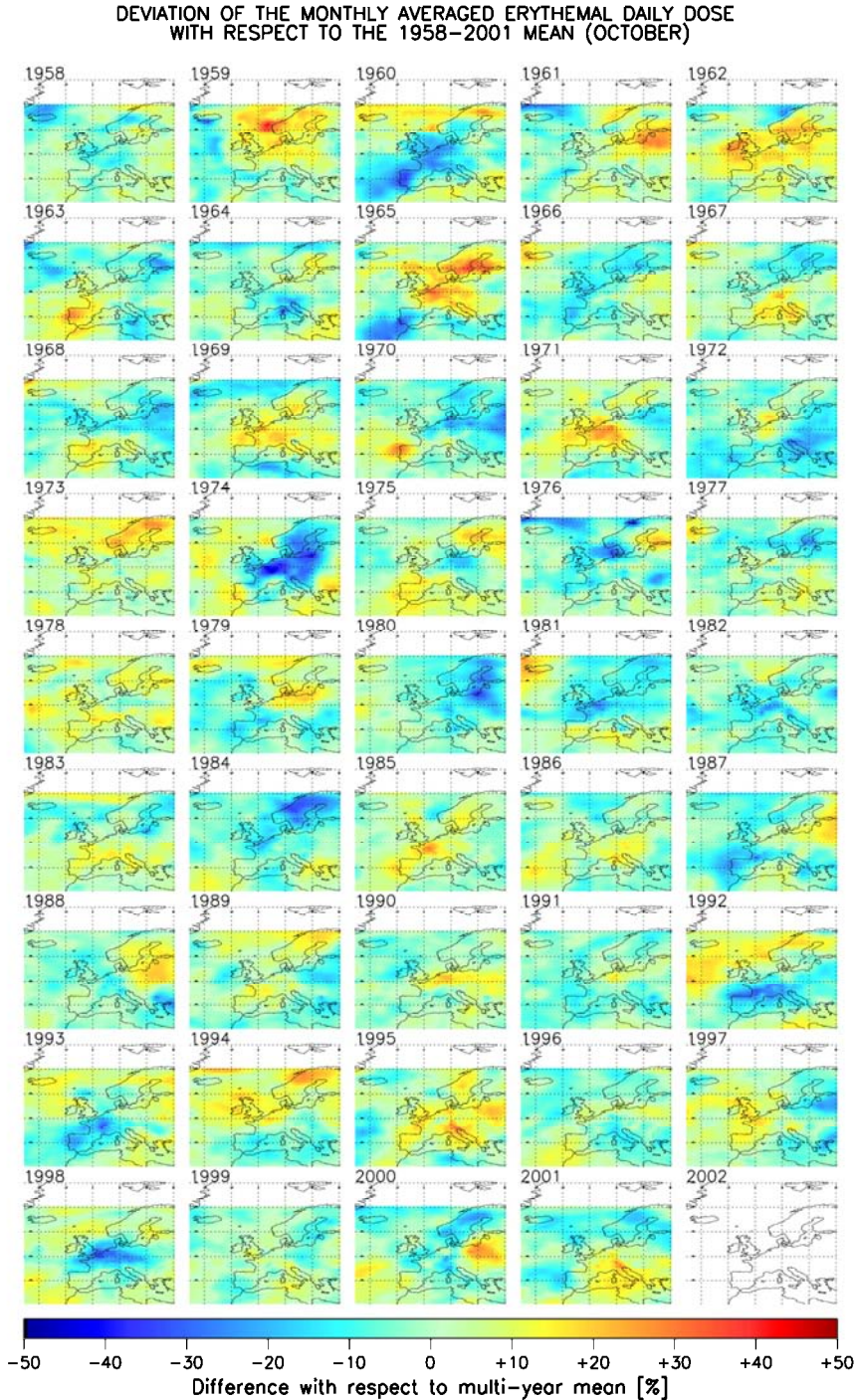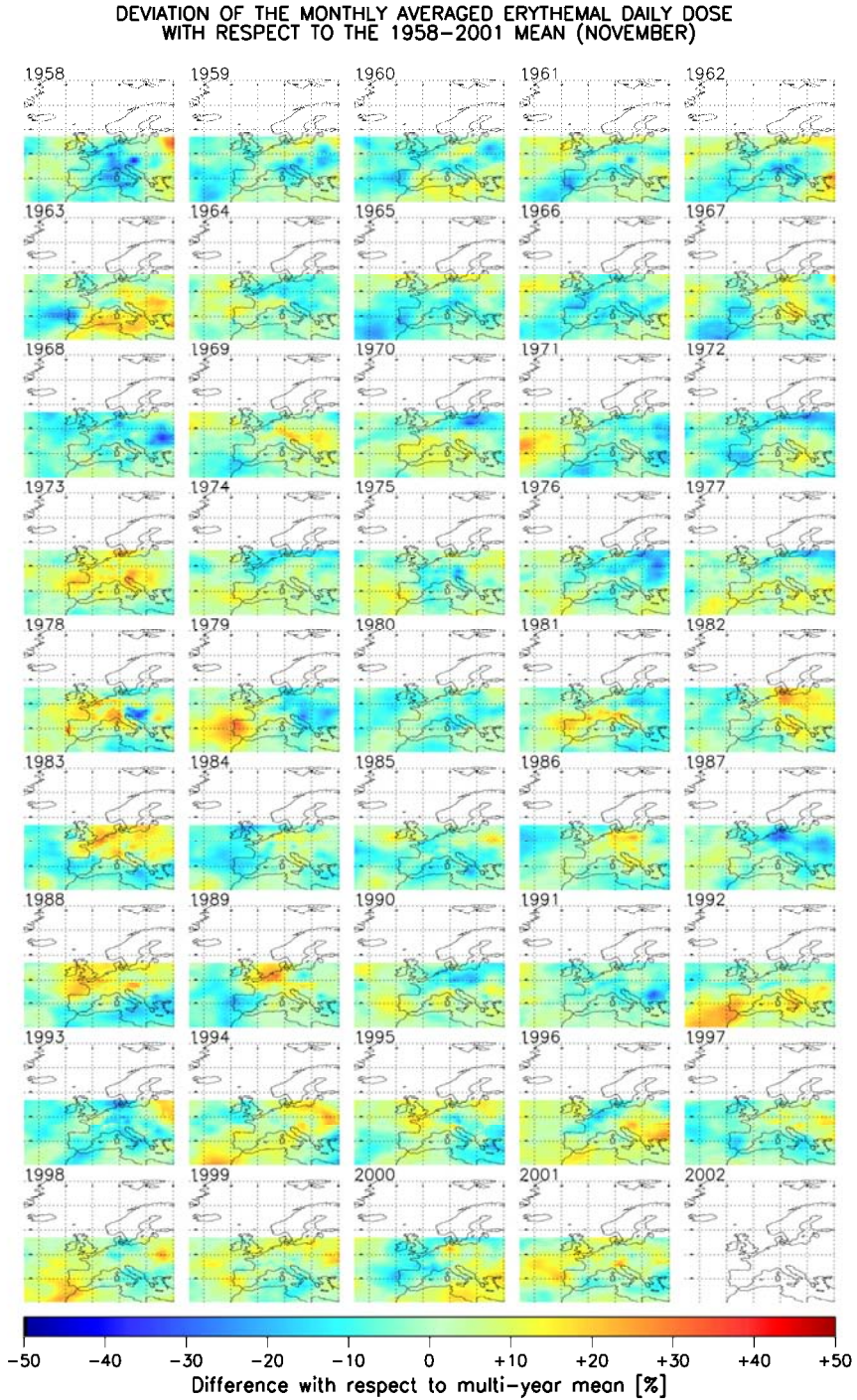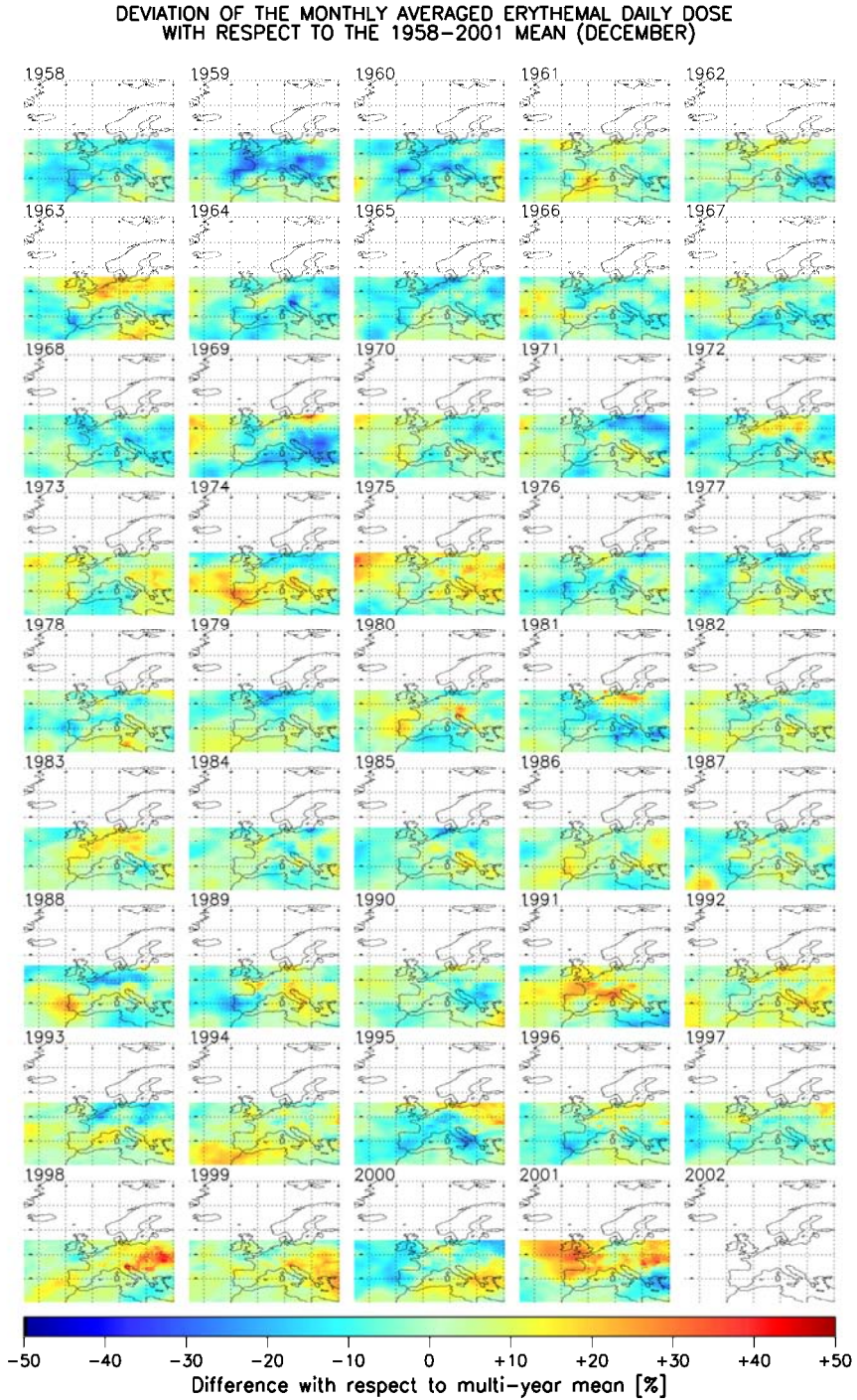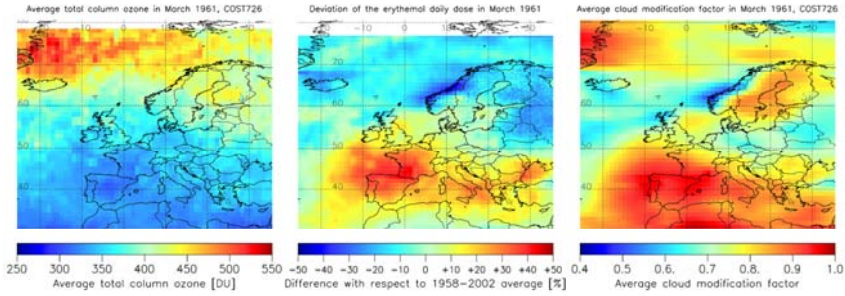
Fig. 6.2.20: March 1961, average total column ozone (left), deviation of the erythemal UV (centre) and average cloud modification factor (right).
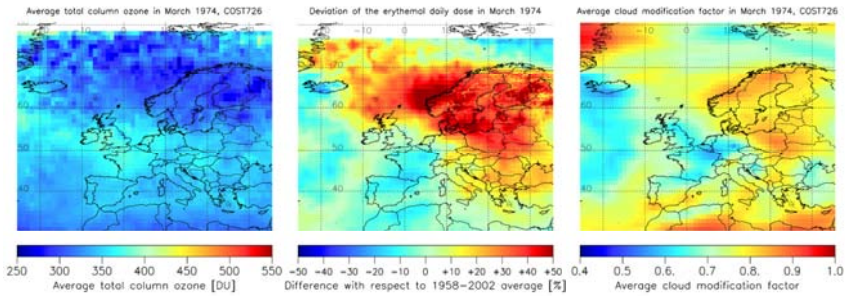
Fig. 6.2.21: March 1974, average total column ozone (left), deviation of the erythemal UV (centre) and average cloud modification factor (right).
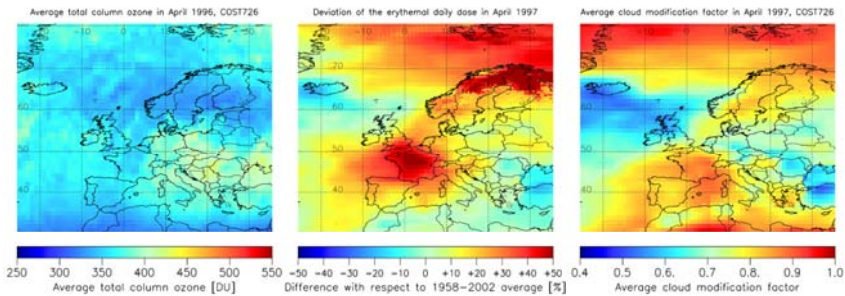
Fig. 6.2.22: April 1996, average total column ozone (left), deviation of the erythemal UV (centre) and average cloud modification factor (right).

The figures above show three cases extracted from the full series, accompanied by the corresponding total column ozone (on the left) and the average cloud modification factor (on the right). In March 1961 (Fig. 6.2.20) the ozone was exceptionally abundant in the North, leading to a deficit in the erythemal radiation, even if the cloudiness was relatively low in the same area. The large excess over Scandinavia and Finland in March 1974 (Fig. 6.2.21) results from the combination of low ozone and low cloudiness. So is the case in April 1996 (Fig. 6.2.22) while the excess over France is caused by low cloudiness, the ozone being close to normal at this latitude.

Fig. 6.2.23: March 10 (top) and July 10 2000 (bottom), CIE 2006 weighted daily dose (left), ratio of CIE 2006 weighted to erythemal daily dose (centre) and total column ozone field (right).

As previously mentioned, the data set also contains daily maps at 7 discrete wavelengths. The purpose of these additional maps is to enable the reconstruction of daily doses corresponding to other effects of UV radiation. An important and beneficial on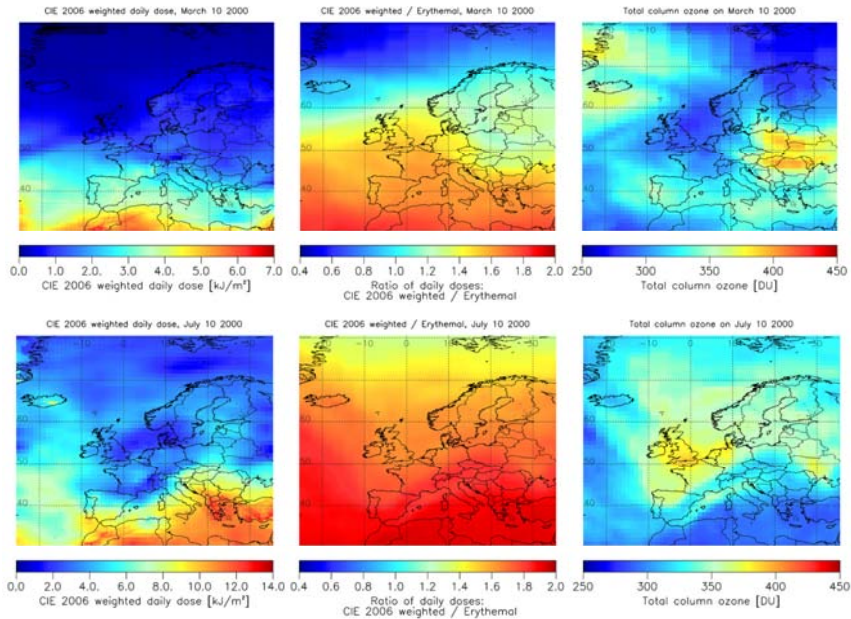e is the photosynthesis in the skin of pre-vitamin D3. Figure 6.2.23 illustrates the UV radiation spectrally weighted for its efficiency with regard to this process. The action spectrum used is the one endorsed by the International Committee on Illumination (CIE 2006). The two images on the on the left represent the CIE 2006 weighted daily dose on March 10 (top) and July 10 2000 (bottom) respectively. The influencing factors are the same as for the erythemal radiation: cloudiness, altitude, surface albedo, aerosols, solar zenith angle and total column ozone. However, the "vitamin D efficient UV" is more sensitive to absorption by ozone than the erythemal radiation. With respect to the erythemal action spectrum, the CIE 2006 action spectrum indeed puts a larger relative weight on shorter wavelengths and is close to zero in the UVA. As a consequence, the "vitamin D efficient UV" decreases with high solar zenith angle more rapidly than the erythemal UV, as the effective path of the photons through ozone gets longer. This shows in the centre images of the panel representing the ratio of CIE 2006 weighted to erythemal daily doses on the two days. In July and at low latitude, this ratio is close to two while it drops below one in the North in March. Obviously this ratio also decreases with the amount of total column ozone itself. One can see that the patterns in the ratio images correspond to the patterns of total column ozone on the corresponding days (images on the right).

6.3 TEMPORAL CHANGE, TREND ANALYSIS – ERYTHEMAL UV

Janusz Krzyścin [a]

a) Polish Academy of Sciences, Institute of Geophysics.

Surface UV exhibits variations in different time scales ranging from minutes up to decades. Such variability reflects many complicated processes affecting UV transmission through the atmosphere. The most pronounced periodical signal in the UV data is the daily and yearly course related to the sun elevation. The highest sun elevation at local noon corresponds usually to the UV maximum. As

reconstructed daily total ozone values are available for Europe since January 1, 1950 it becomes possible to estimate all-sky modelled UV radiation for sites providing global solar radiation from measurements that allows to estimate cloud correction of the clear-sky UV irradiances calculated on the basis of total ozone data and other variables fixed to their climatological means. There are many weather stations that measure routinely global radiation using pyranometers. Stations providing long series (~50 years) of the solar measurements are of special interest in discussion of the multi-scale UV variability. The interest on UV temporal variations encompasses mostly a prediction of next-day daily maximum (UV index) or an extraction of persistent tendency from the time series. In this chapter, we will focus on calculations of the long-term changes in the reconstructed UV data.

One of the objectives of COST 726 was examination of the European UV reconstruction models (Koepke et al., 2008). Following models have been found within the group of best performing models when compared with the measured erythemally weighted UV daily doses: Geophysical Institute, Slovak Academy of Sciences (GSAS), Bratislava, Slovakia; Institute of Meteorology and Water Management (IMGW), Warsaw, Poland; National Institute for Public Health and the Environment (RIVM), Bilthoven, the Netherlands. Here we discuss the temporal UV variability for some reconstruction sites using output of these models. For example, figure 6.3.1 shows the reconstructed (GSAS model) UV series for Budapest starting in January 1, 1950. Moreover, we examine the spatial distribution of long-term UV changes and its forcing factors over Europe using COST 726 maps with 1° × 1° resolution.
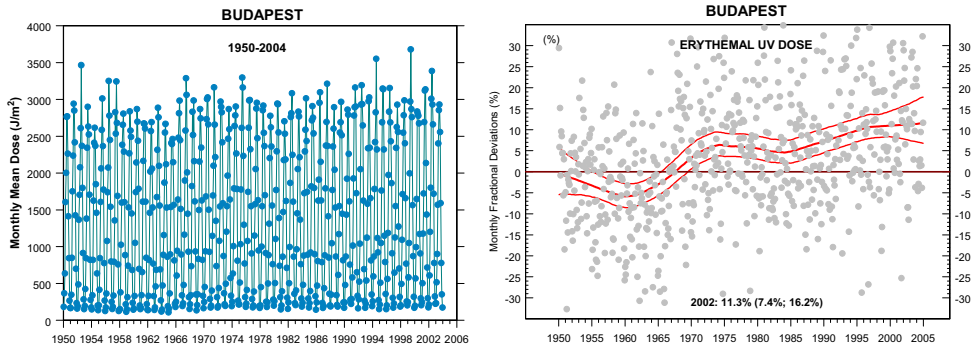

Fig. 6.3.1: Monthly mean doses from the reconstructed (GSAS model) daily erythemaly weighted doses for Budapest since January 1950 – (left), smooth curve fitted to monthly fractional deviations with 95 % uncertainty range to illustrate trend pattern and its uncertainty – (right).

In multi-scale analysis of the data it is convenient to use monthly fractional deviations, i.e., deviations of actual monthly means from the long-term monthly means expressed in percent of these long-term means. In this way, the strong yearly course is subtracted from the data. Next, a spectral analysis is performed to separate the variability in selected time scales. Wavelet decomposition allows not only identifying periodicities of the original signal but also the amplitudes of the signal multiscale components. Figure 6.3.2 shows the wavelet decomposition of the monthly fractional deviations for Budapest derived from the reconstructed UV data by the GSAS model. The low frequency components (with time scale >10 years) of the wavelet decomposition are summed to form a trend component. The trend pattern for Budapest shows two periods with positive tendency (1960–1975 and since 1985). Further in the text we will analyze the UV level in 2002 that is taken from the trend pattern extracted from various fractional deviations (individual stations, maps).
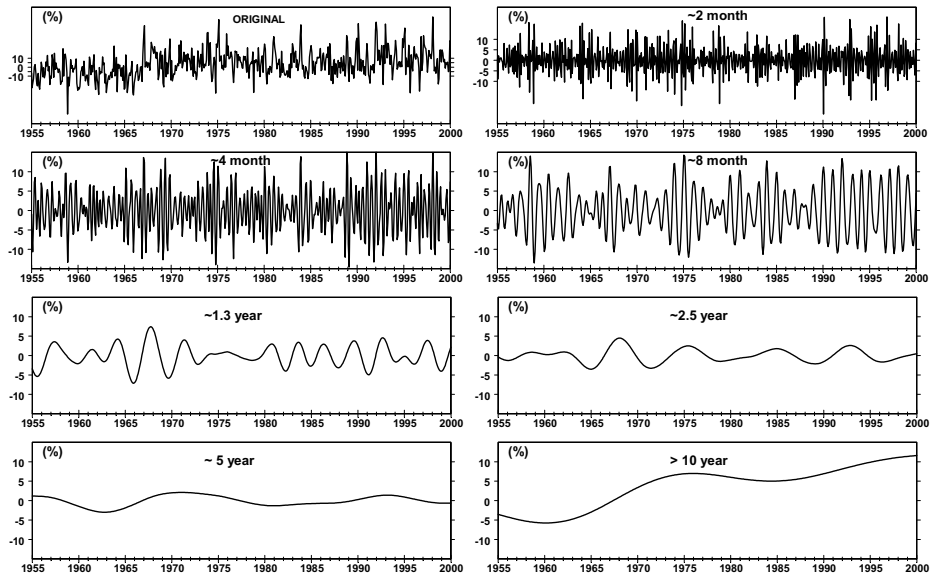
Fig. 6.3.2: Wavelet decomposition of the monthly fractional variations taken from reconstructed (GSAS model) erythemaly weighted doses for the period 1950-2004 in Budapest.

The long-term variability is usually extracted from a straight line fit to the whole analyzed time series or its subsets (e.g., Reinsel et al., 2002; WMO, 2003). A comparison of slopes of the regression lines enables to infer temporal variations of the long-term component of time series. Recently a concept of trend evaluation using a smooth curve fit to the data has been developed (Harris et al., 2003; Krzyścin et al., 2005; Oltmans et al., 2006; and Krzyścin, 2006). In such an approach, a trend component means a continuous and smooth pattern extracted from the time series, i.e., the pattern is not a priori assumed. A model using such concept is the so-called flexible trend model and it is also used here. The 95 % confidence ranges for the trend curve uncertainty are derived by block bootstrapping (Krzyścin and Borkowski, 2008).

Tables 6.3.1 and 6.3.2 show the departures of the monthly values of the erythemaly weighted UV, CMF, and ozone in 2002 relative to the base-line level of the variables (long-term monthly means before 1979) in percent of the base-line value. Table 6.3.1 presents the results obtained by GSAS and IMGW model for Budapest (reconstructed UV time series since 1950), Uccle (since 1951), and Tartu (since 1950). Table 6.3.2 contains results by RIVM model for Budapest (since 1950), Hamburg (since 1950), Hohenpeissenberg (since 1953), Potsdam (since 1950), Uccle (since 1951), Warsaw (since 1961), and Zakopane (since 1958). It can be inferred from the models output comparison for Budapest and Uccle that the results by various models are almost equivalent. The models provide the same significance of the estimated values for all sites and seasons. There are slight differences between the mean value estimates. Most of them are within the 95 % confidence interval.

Table 6.3.1: Departure of the reconstructed erythemally weighted radiation (UV), cloud modification factor (CMF$_{UV}$), and column amount of ozone (Ozone) in 2002 relative to the long-term mean (before 1979) in percent of the long term mean for warm sub-periods (April-September), cold periods (October-March), and the whole year (January-December). 95 % confidence ranges of the estimates are in the parentheses. Asterisks mark statistically significant results.

GSAS model

Site	UV	CMF$_{UV}$	Ozone
April-September			
Budapest	6.4*(2.5, 10.5)	3.2 (-0.2, 6.3)	-2.4*(-4.0, -0.8)
Tartu	3.5 (-1.2, 8.4)	1.0 (-2.8, 4.6)	-2.6*(-4.4, -0.9)
Uccle	7.9*(2.7,13.6)	3.4 (-0.2, 8.0)	-3.4*(-5.4, -1.7)
October-March			
Budapest	16.3*(11.4,23.1)	10.0*(5.2, 15.2)	-4.1*(-6.4, -2.1)
Tartu	-6.5*(-11.8,-1.4)	-8.5*(-12.1,-4.6)	-3.0*(-5.9, -0.7)
Uccle	6.5*(2.2, 10.5)	0.9 (-3.2, 5.0)	-4.6*(-6.9, -2.4)
January-December			
Budapest	11.3*(7.4, 16.2)	6.6* (3.0,10.4)	-3.3*(-4.9, -1.8)
Tartu	-1.7 (-5.3, 2.3)	-3.8*(-6.6,-0.8)	-2.8*(-4.7, -1.1)
Uccle	7.2*(3.7, 11.8)	2.3 (-0.3, 5.9)	-4.0*(-5.9, -2.5)

IMGW model

Site	UV	CMF$_{UV}$	Ozone
April-September			
Budapest	5.9*(1.7, 9.4)	2.6 (-0.2, 5.1)	-2.3*(-4.0, -0.8)
Tartu	4.2 (-0.9, 9.1)	1.4 (-2,1, 4.7)	-2.6*(-4.5, -0.8)
Uccle	7.9*(3.1,13.3)	3.0 (-0.3, 6.9)	-3.4*(-5.2, -1.8)
October-March			
Budapest	21.7*(15.3,29.4)	11.8*(6.3, 17.7)	-4.1*(-6.3, -2.2)
Tartu	-6.6*(-13.4,-1.3)	-9.3*(-14.1,-4.2)	-3.0*(-5.9, -0.7)
Uccle	10.4*(5.9, 15.1)	3.5 (-0.5, 7.9)	-4.6*(-6.8, -2.5)
January-December			
Budapest	13.6*(9.8, 18.8)	7.2* (3.6,10.8)	-3.3*(-5.0, -1.8)
Tartu	-1.3 (-5.6, 4.0)	-4.2*(-7.3,-0.8)	-2.8*(-4.9, -1.1)
Uccle	9.5*(5.8, 13.4)	3.2* (0.8, 7.1)	-4.1*(-5.9, -2.4)

Higher UV levels in 2002 by ~5-10 % than those before satellite era (pre-1979) are found over many stations. However, such increase is the most pronounced for stations located in large urban regions. The differences between the reconstructed UV levels over the stations are mainly induced by the local properties of cloud/aerosol forcing. Ozone drives a smooth increase of UV since the early 1980s. The level in 2002 is about 3–5 % higher than that before 1979 due to the ozone forcing. Long-term increase of the atmosphere transparency induced by changes in cloud/aerosol properties is especially pronounced for Budapest in cold seasons and Warsaw in all seasons. Both ozone and cloud/aerosol effects induce a high increase of the present mean UV level up to ~15 % in Budapest. Over Tartu and Zakopane we have found the opposite effects in the cold sub-periods and the mean UV level in 2002 is the lowest in the record with ~5 % deficit. The statistically significant decline of UV at the end of the time series has been found in